ADVANCING EARTH AND SPACE SCIENCE

Journal of Advances in Modeling Earth Systems

RESEARCH ARTICLE
10.1029/2017MS001213

Key Points:
- Iterative dynamic initialization for whole atmospheric global modeling is presented
- Gravity wave momentum forcing and mass circulations are estimated to constrain nudging coefficient
- Deviations from nonlinear balance may occur in association with large-scale instabilities

Supporting Information:
- Supporting Information S1

Correspondence to:
I.-S. Song,
isong@kopri.re.kr

Citation:
Song I.-S., Chun, H.-Y., Jee, G., Kim, S.-Y., Kim, J., Kim, Y.-H., & Taylor, M. A. (2018). Dynamic initialization for whole atmospheric global modeling. *Journal of Advances in Modeling Earth Systems*, *10*, 2096–2120. https://doi.org/10.1029/2017MS001213

Received 23 OCT 2017
Accepted 16 JUL 2018
Accepted article online 24 JUL 2018
Published online 3 SEP 2018

Dynamic Initialization for Whole Atmospheric Global Modeling

I.-S. Song[1], H.-Y. Chun[2], G. Jee[1], S.-Y. Kim[3], J. Kim[3], Y.-H. Kim[4], and M. A. Taylor[5]

[1]Korea Polar Research Institute, Incheon, South Korea, [2]Department of Atmospheric Sciences, Yonsei University, Seoul, South Korea, [3]Korea Institute of Atmospheric Prediction Systems, Seoul, South Korea, [4]Institute for Atmospheric and Environmental Sciences, Goethe University Frankfurt, Frankfurt am Main, Germany, [5]Sandia National Laboratories, Albuquerque, NM, USA

Abstract An iterative dynamic initialization method is presented to produce balanced initial conditions for whole atmospheric global modeling. In this method, a global hydrostatic numerical model is iteratively nudged toward ground-to-space wind and temperature profiles at specific date and time. Ground-to-space atmospheric profiles are obtained by fitting spline curves to reanalyses below the lower mesosphere and empirical model results in the upper atmosphere. An optimal nudging coefficient is determined by examining if reasonable structure of mesospheric gravity wave (GW) momentum forcing and residual mean meridional circulations can be obtained from balanced initial conditions. Estimated mesospheric GW momentum forcing is found to exhibit a distinctive structure with larger (smaller) values in the lower and upper mesosphere (in the midmesosphere), when compared with parameterized climatological forcing. The iterative dynamic initialization allows for dynamical balance among the model's prognostic variables and reduces excitation of spurious GWs and noises at initial time. However, theoretical imbalances, measured by the ellipticity of the nonlinear balance equation, are not completely eliminated in balanced flows, and they are found in narrow tropospheric frontal regions and over localized areas associated with the large-scale instability in the midlatitude middle atmosphere. These imbalances are discussed in the context of their potential relation to generation of planetary-scale and inertia GWs around the middle atmospheric and tropospheric jets.

Plain Language Summary This study reports a method of initializing a whole-atmosphere global model that covers from the ground to the lower thermosphere. Through this initialization, a whole atmospheric state balanced with the model dynamics is effectively generated. Free coefficient required for the initialization is chosen by estimating gravity wave momentum forcing and meridional mass circulations in the mesosphere and lower thermosphere. In the generated balanced flow, theoretical imbalances, measured by the ellipticity of the nonlinear balance equation, are found. These imbalances can be related to the spontaneous generation of gravity waves and balanced and unbalanced large-scale instabilities in the middle atmosphere. The large-scale instabilities can be attributed to generation of the planetary-scale and inertia gravity waves in the middle atmosphere.

1. Introduction

As is well known through the history of numerical weather prediction (NWP), appropriate initialization of numerical models is crucial for accurate simulation of the evolution of atmospheric flows (Daley, 1991; Kalnay, 2003; Warner, 2011). Spatiotemporal structure of winds and thermodynamic state variables to be used to initialize models should be consistent with the dynamics of slowly varying large-scale flows to avoid meteorologically insignificant high-frequency oscillations such as sound waves or fast-moving gravity waves (GWs) that may deteriorate modeling results (e.g., Baer & Tribbia, 1977; Errico, 1982; Ford et al., 2000; Leith, 1980; Lorenz, 1980; Warn et al., 1995). Such a slowly varying flow is often referred to as the balanced flow and described by a diagnostic balance relation and time evolution of the potential vorticity (PV) (McIntyre, 2015a; Plougonven & Zhang, 2014; Vanneste, 2013). Slowly varying large-scale wind and mass (temperature and geopotential) fields can be inverted from the PV field, and therefore examining spatiotemporal PV evolution is essential to comprehend characteristics of the large-scale atmospheric flow (Hoskins et al., 1985; McIntyre, 2015b).

Below the lower mesosphere, global distributions of balanced atmospheric fields can be obtained at a regular time interval of 3 or 6 hr from operational data assimilation products such as European Centre for Medium-Range Weather Forecasts (ECMWF) Interim reanalysis (ERA-Interim, hereafter; Dee et al., 2011) and NASA's Modern-Era Retrospective Analysis for Research and Application (MERRA; Bosilovich et al., 2015; Rienecker et al., 2011). These products are substantially constrained by various in situ and remote sensing observations (see Fujiwara et al., 2017, for details) and have been considered to be reliable such that they can often be used as proxies for observations, although they may in fact have systematic biases in several aspects (e.g., Dolinar et al., 2016; Kawatani et al., 2016; Nygård et al., 2016). In the mesosphere and lower thermosphere (MLT) region (the lower part of the upper atmosphere), however, it is not easy to obtain global distributions of balanced atmospheric variables at such a regular time interval as in the lower atmosphere. Some analysis data provide information up to the upper mesosphere, but their temporal resolution or available time period is still limited. UK Met Office stratospheric and mesospheric analyses ($z < 80$ km; Long et al., 2013; Swinbank & O'Neill, 1994) are open to the public only for data at 1200 UT (once a day). Naval Research Laboratory high-altitude data assimilation products ($z < 97$ km; Eckemann et al., 2009) are accessible to external users only for particular time periods. Other than these products, various high-altitude data assimilations have been attempted by extending an operational data assimilation system (Wang et al., 2011) or by applying a stand-alone ensemble-based system in a whole-atmosphere model (Pedatella et al., 2014) for research purposes for particular time periods.

Limited spatiotemporal coverage of whole atmospheric analysis data may be overcome for particular purposes such as ray-tracing modeling of acoustic waves as in Ground-to-Space (G2S) specification in Drob et al. (2003). G2S specification produces whole atmospheric vertical profiles of winds and thermodynamic state variables through data fusion achieved by fitting B-spline curves given as a function of heights to NWP products in the troposphere and stratosphere and statistical information about spatiotemporal variations of neutral winds and temperature in the upper atmosphere. In Drob et al. (2003), upper-atmospheric statistical information is obtained from empirical models such as Mass Spectrometer and Incoherent Scatter radar empirical model (MSIS-90) for temperature and density (Hedin, 1991) and Horizontal Wind Model (HWM-93) for horizontal winds (Hedin et al., 1996). These models provide results obtained by fitting horizontally global and vertically localized basis functions to multidecadal (ground, rocket, and satellite) observations, and they can reproduce major characteristics of the neutral dynamics and thermal and chemical states in the upper atmosphere (e.g., thermally driven mean circulations; the antisunward flow and two-cell convections associated with the electrostatic potential in the polar regions; subdaily variations such as diurnal, semidiurnal, and terdiurnal migrating tides; and distributions of various gas densities) and their dependencies on solar and geomagnetic activities (see Burns et al., 2014; Forbes, 2007; Fuller-Rowell, 2013).

Data fusion in G2S specification, however, results in abrupt variations in spectral structure of the atmospheric flows in the vertical direction around altitude ranges where different kinds of data are merged with one another. That is, amplitudes and properties of atmospheric waves in G2S profiles may be discontinuous in the vertical direction. It is evident that large discontinuities occur in the MLT region due to substantially low horizontal resolution (up to zonal wave number 3) of the empirical models' spherical harmonic formulations (see Drob et al., 2015; Emmert et al., 2008; Hedin, 1991, for details) compared with fine horizontal resolutions (0.5–2.5°; see Nygård et al., 2016; Fujiwara et al., 2017) of assimilation products in the lower atmosphere. More important, whole atmospheric data constructed through data fusion may lead to several issues when they are used in dynamical modeling because the constructed data may not respect the atmospheric dynamics. Initial conditions to be used in dynamical modeling should not simply be specified through interpolation of atmospheric data (Daley, 1991; Kalnay, 2003). As mentioned earlier, models should at least be initialized with balanced states consistent with model dynamics (Daley, 1991), although data assimilation ultimately requires initial conditions to be optimal states in which observational and model states and individual errors are comprehensively reflected (Bloom et al., 1996; Lorenc, 1986; Lorenc et al., 1991).

In this study, we generate whole atmospheric balanced states using an iterative initialization method based on nudging (see Cacuci et al., 2014; Lakshmivarahan & Lewis, 2013, for reviews). For this, we first construct global G2S atmospheric profiles, covering from the ground to the thermosphere, at specific date and time, benchmarking the G2S specification in Drob et al. (2003). Then, to obtain balanced states at specific time, a primitive equation model is iteratively nudged toward G2S profiles at a specific time until certain criteria are satisfied. Nudging (i.e., Newtonian relaxation) has widely been employed in both regional and global modeling because of its simplicity in formulation and implementation (e.g., Auroux & Blum, 2008; Bao & Errico, 1997;

Bloom et al., 1996; Davies & Turner, 1977; Hoke & Anthes, 1976, 1977; Krishnamurti et al., 1991; Lorenc et al., 1991; Telford et al., 2008; Zou et al., 1992). However, the conventional nudging method is different from ours in that it usually drives a model to proceed forward in time toward given time sequence of data rather than iteratively nudge the model toward data at a specific time. Since nudging requires dynamical prediction models, the conventional method is called the dynamic initialization. Our method is referred to as the iterative dynamic initialization to distinguish from the conventional one. In our initialization, we define the term *balanced states* in a practical sense as atmospheric states consistent with model dynamics so that excitation of spurious high-frequency GWs can be minimized as described in Daley (1991). In a theoretical sense, however, balanced states can be more precisely defined by slowly varying large-scale flows described by balance relations and PV dynamics. Hence, we quantitatively check how much the theoretical balance is achieved in balanced fields generated through the iterative dynamic initialization, using the nonlinear balance equation and its ellipticity condition (Bourchtein & Bourchtein, 2010; Houghton, 1968; Kasahara, 1982).

This paper is organized as follows: Section 2 illustrates how G2S atmospheric profiles are produced. Section 3 describes a global hydrostatic dynamical model used in this study. Section 4 accounts for how balanced states are generated through iterative dynamic initialization and demonstrates characteristic properties of the generated balanced states. In section 5, we discuss theoretical imbalances in the generated balanced flow in the troposphere and midlatitude middle atmosphere and their potential roles in the atmospheric dynamics. Summary and conclusion is given in section 6.

2. Global G2S Atmospheric Profiles

Global G2S atmospheric profiles are obtained as a function of pressures (*ps*) for the following variables: zonal and meridional wind components (u and v), air temperature (T), specific humidity (q), and specific contents for hydrometeors such as liquid cloud (q_c) and cloud ice (q_i). Below the lower mesosphere, variables are acquired from the ERA-Interim and MERRA data sets. The standard pressure level versions of these data sets extend from 10^3 up to 1 hPa for the ERA-Interim and up to 0.1 hPa for the MERRA. These two data sets with different biases and vertical coverage are used to obtain more robust analysis data that include the middle atmosphere as much as possible. For the ERA-Interim data, variables are defined below the ground (i.e., between 10^3 hPa and the ground) through postprocessing procedure (e.g., Haseler & Sakellarides, 1986), and hence all the values of the variables from 10^3 to 1 hPa are utilized in construction of the G2S atmospheric profiles. For the MERRA data where values below the ground are set undefined, variables above 400 hPa (i.e., 400–0.1 hPa) are only employed. Between 400 and 1 hPa, both ERA-Interim and MERRA data are used. Hydrometeor variables q_c and q_i are not provided in MERRA, and therefore only the ERA-Interim data below 1 hPa are used for q_c and q_i.

Above 1 hPa ($z \approx 50$ km), empirical model results are used to specify atmospheric profiles, and they are partially overlapped by the MERRA data below 0.1 hPa ($z < 60$ km). For horizontal winds, the HWM14 model (Drob et al., 2015) is used. The HWM14, a major update to the HWM07 (Drob et al., 2008), gives complete horizontal winds by adding geomagnetically disturbed winds computed from the DWM07 (Emmert et al., 2008) to quiet time winds. Disturbed winds are added only when the 3-hourly geomagnetic (*Ap*) index is nonzero. Quiet time HWM14 winds represent the zonal-mean wind, stationary planetary waves, and three harmonics of the migrating (Sun-synchronous) tides. For temperature, the NRLMSISE-00 model (Picone et al., 2002) is used. The NRLMSISE-00 model provides densities of atmospheric constituents (O, N_2, O_2, Ar, H, and N), total air density (ρ), and temperature. These quantities depend on solar and geomagnetic activities represented by the daily $F_{10.7}$ index and 3-hourly (and daily averaged) *Ap* indices, respectively. In the HWM14, dependence on solar activities is currently missing, which is one of the future directions for improvements (see Drob et al., 2015, for details). Specific humidity (q) and information about hydrometeors (q_c and q_i) are not provided by the empirical models and thus set equal to 0 in the altitudes covered by empirical models.

Vertically continuous G2S atmospheric profiles are constructed by fitting B-spline curves to reanalyses in the lower atmosphere and empirical model results in the upper atmosphere. Details of the construction procedure are described in Appendix A.

Figure 1 shows zonal wind and temperature obtained from the ERA-Interim, MERRA, and empirical models at 54°S and 60°W at 0000 UT on 1 July 2014 and curves fit to the three kinds of data. The curves smoothly pass through reanalysis data and empirical model results, which indicates that they may represent reasonably whole atmospheric vertical profiles of winds and temperature at specific horizontal location and time.

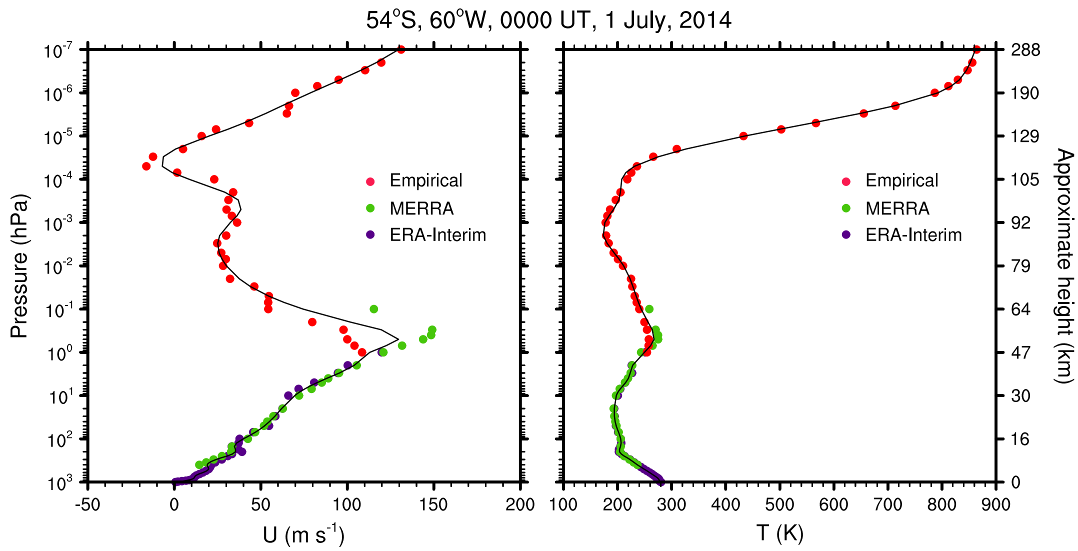

Figure 1. Zonal wind and temperature obtained from (purple) the ERA-Interim, (green) MERRA, and (red) empirical models at 54°S and 60°W at 0000 UT on 1 July 2014 and (black solid line) the G2S curves fit to those data. ERA-Interim = European Centre for Medium-Range Weather Forecasts (ECMWF) Interim reanalysis; MERRA = Modern-Era Retrospective Analysis for Research and Application; G2S = ground-to-space.

The zonal wind profile shows the polar night jet near 1 hPa and the reversed (i.e., westward) jet near 10^{-4} hPa, which is typical wind structure in the winter high-latitude regions. The temperature profile demonstrates the layered structure of the atmosphere, characterized by vertical temperature gradients. The tropopause, stratopause, and mesopause are located around 100, 1, and 10^{-3} hPa, respectively. Thermospheric temperature reaches 850 K near $z = 300$ km. Given that 0000 UT at the geographical location (the winter hemisphere) chosen in Figure 1 roughly corresponds to 2000 LT (nighttime), temperature of 850 K may be close to the lower bound of thermospheric temperature. In solar maximum, thermospheric temperature may reach up to 1100 K, whereas in minimum, it may be lowered to about 750 K (Schunk & Nagy, 2009).

Figure 2 demonstrates latitude-height cross sections of G2S zonal wind and temperature at 60°W at 0000 UT on 1 July 2014. The G2S zonal wind exhibits a characteristic structure: subtropical tropospheric jets in both hemispheres, the westward wind phase of the quasi-biennial oscillation in the equatorial lower stratosphere, polar night jets tilted toward the equator in the stratosphere and lower mesosphere, westward jets in the summer middle atmosphere, and wind reversals near the mesopause in both hemispheres. The eastward jet is gradually changed to the westward wind across the mesopause in the winter hemisphere, whereas opposite wind reversal in the summer hemisphere occurs rapidly in the vertical direction at the lower altitudes. This is related to the fact that the mesopause in the summer hemisphere is located at the lower altitudes than in the winter hemisphere (A. K. Smith, 2012). This seasonal difference in the mesopause height is clearly seen in G2S temperature structure (Figure 2b). Local minimum temperatures at the mesopause are found near $z = 80$ km in the summer polar region and near $z = 90$ km in the winter midlatitude region. G2S temperature also reproduces typical structure: warm regions in the upper stratosphere due to the ozone UV absorption, cold regions in the equatorial lower stratosphere associated with the Brewer-Dobson circulation, and substantially cold regions in the polar lower stratosphere in the winter hemisphere (Andrews et al., 1987).

3. Global Dynamical Model

Dynamically balanced atmospheric states in this study are obtained using a global dynamical model iteratively nudged toward G2S atmospheric profiles described in the previous section. The dynamical model used in this study adopts the spectral element (SE) hydrostatic dynamical core implemented in National Center for Atmospheric Research Community Atmosphere Model (Taylor, 2011). The SE core is based on a continuous Galerkin spectral finite-element method (Taylor & Fournier, 2010; Taylor et al., 1997) in horizontal discretization. A globally quasi-uniform cubed-sphere (CS) grid is chosen for implementation of the SE core in the global model. In the CS grid, the six faces of a cube are mapped onto the spherical surface using

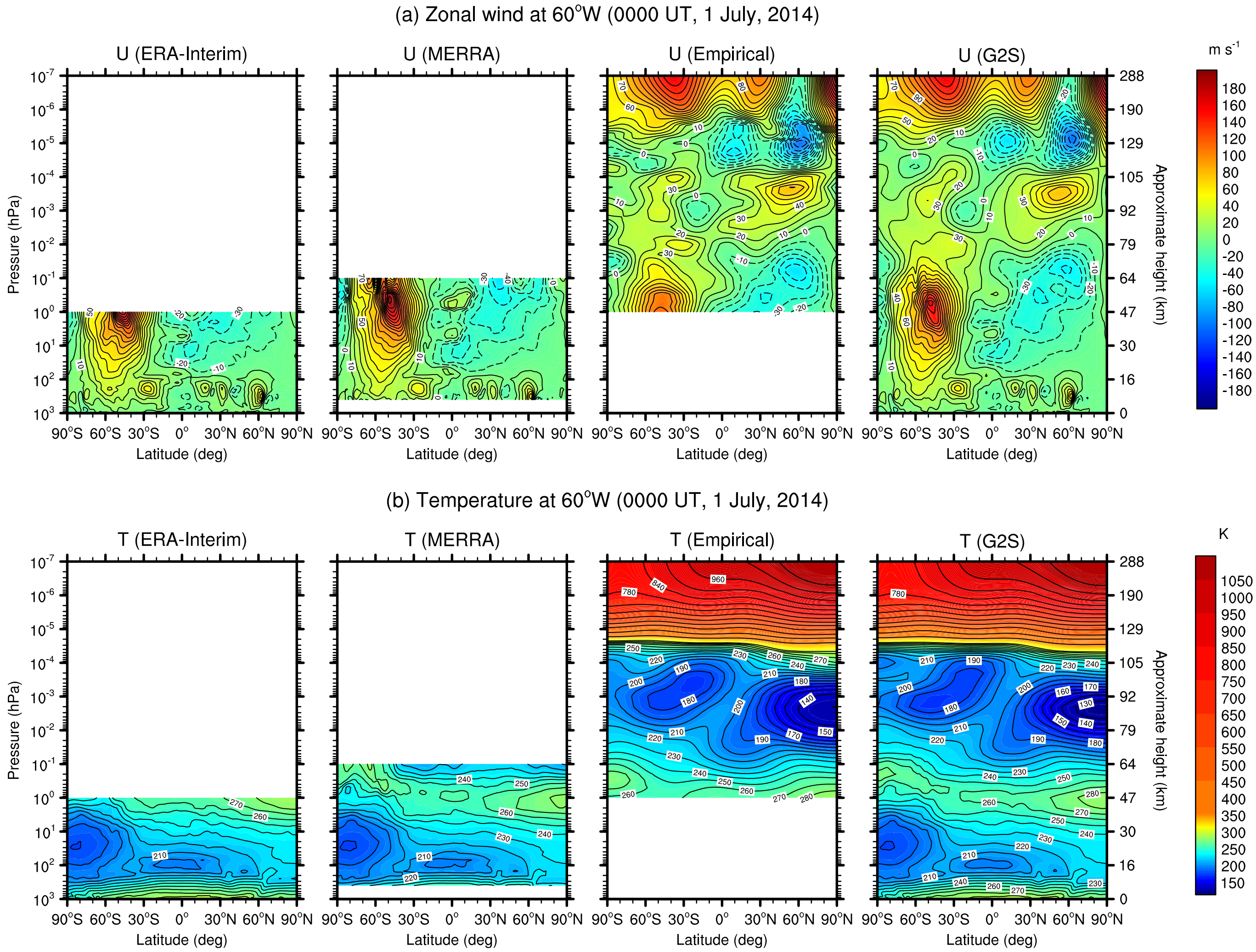

Figure 2. Latitude-height cross sections of (a) zonal wind and (b) temperature in the ERA-Interim, MERRA, empirical models, and G2S data at 60°W at 0000 UT on 1 July 2014. For zonal wind, shading and contour intervals are 2 and 10 m/s, respectively. Contours for westward wind are plotted in dotted lines. For temperature, shading interval is 5 (100) K below (above) 360 K, and contour interval is 10 (60) K below (above) than 290 K. ERA-Interim = European Centre for Medium-Range Weather Forecasts (ECMWF) Interim reanalysis; MERRA = Modern-Era Retrospective Analysis for Research and Application; G2S = ground-to-space.

the equiangular central projection (Rančić et al., 1996). Continuous Galerkin method allows for a simple projection operator that generates continuous data values across the element boundaries using data values only at Gauss-Lobatto-Legendre quadrature points along element boundaries. This property helps the SE core achieve excellent parallel performance in massively parallel computing environments because communication occurs only through element boundaries shared by adjacent elements (Dennis et al., 2012; Taylor et al., 2008).

The SE core numerically solves primitive equations for horizontal momentum, temperature, pressure, and constituents in the terrain-following hybrid η vertical coordinate (Kasahara, 1974; Simmons & Burridge, 1981). The primitive equations are obtained under the spherical geopotential, shallow-atmosphere, and hydrostatic approximations (White et al., 2005) and can be written, neglecting the horizontal diffusion terms, as follows:

$$\frac{\partial \boldsymbol{u}}{\partial t} + \left(\zeta + f\right) \boldsymbol{k} \times \boldsymbol{u} + \boldsymbol{\nabla}\left(\frac{|\boldsymbol{u}|^2}{2} + \Phi\right) + \dot{\eta}\frac{\partial \boldsymbol{u}}{\partial \eta} + \frac{RT_v}{p}\boldsymbol{\nabla} p = \boldsymbol{P_u} + \boldsymbol{A_u}, \tag{1}$$

$$\frac{\partial T}{\partial t} + \boldsymbol{u} \cdot \boldsymbol{\nabla} T + \dot{\eta}\frac{\partial T}{\partial \eta} - \frac{RT_v}{c_p^* p}\omega = P_T + A_T, \tag{2}$$

$$\frac{\partial}{\partial t}\left(\frac{\partial p}{\partial \eta}\right) + \nabla \cdot \left(\frac{\partial p}{\partial \eta}\boldsymbol{u}\right) + \frac{\partial}{\partial \eta}\left(\frac{\partial p}{\partial \eta}\dot{\eta}\right) = 0, \tag{3}$$

$$\text{and } \frac{\partial}{\partial t}\left(\frac{\partial p}{\partial \eta}q\right) + \nabla \cdot \left(\frac{\partial p}{\partial \eta}q\boldsymbol{u}\right) + \frac{\partial}{\partial \eta}\left(\frac{\partial p}{\partial \eta}q\dot{\eta}\right) = 0. \tag{4}$$

Here $\boldsymbol{u}$ is the horizontal wind vector. T is the temperature; q denotes the specific humidity or specific contents of hydrometeors and chemical constituents. ∇ is the horizontal differential operator. The ζ ($= \boldsymbol{k} \cdot \nabla \times \boldsymbol{u}$) is the vertical component of the relative vorticity. The f is the Coriolis parameter given by $2\Omega \sin \phi$. Ω is the angular frequency of the Earth's rotation. The ϕ is the latitude. The $\boldsymbol{k}$ is the unit vector normal to the spherical surface. Φ is the geopotential computed using the hydrostatic relation. The $\dot{\eta}$ is the vertical velocity across the η coordinate. R is the gas constant for dry air. T_v is the virtual temperature. The p is the moist pressure that satisfies the ideal gas law $p = \rho R T_v$, where ρ is the air density. The ω ($= Dp/Dt$) is the pressure vertical velocity. The c_p^* is given by $c_p + (c_{pv} - c_p)q$ where c_p and c_{pv} are specific heats for dry air and water vapor, respectively. $\boldsymbol{P_u}$ and P_T are physics forcing terms for momentum and temperature, respectively. $\boldsymbol{A_u}$ and A_T denote assimilation terms used to constrain the model so that the model can generate a balanced flow at a specific date and time. Time integration of (1)–(4) is described in detail in Appendix B.

The primitive equations are based on two core approximations: The shallow-atmosphere and hydrostatic approximations. Although whole-atmosphere modeling is the topic of this study, the use of the shallow-atmosphere approximation (Phillips, 1966) is likely to be acceptable, given that the highest model layer is located at $z \approx 135$ km. A maximum relative error of approximating the radius r ($= a+z$) from the center of the Earth using the mean radius of the Earth a is about 2.2% at the model top layer. If the model is vertically extended beyond the middle thermosphere, deep-atmosphere formulations may be required (see White et al., 2005). On the other hand, the use of the hydrostatic approximation may possibly be an issue, given that substantially large vertical winds can occur in the thermosphere (Schunk, 2012). Large vertical velocities are hardly accounted for by mass conservation based on the hydrostatic assumption (e.g., Anderson et al., 2011; Larsen & Meriwether, 2012; R. W. Smith & Hernandez, 1995). There are still uncertainties in mechanisms of such strong vertical motions. A potential mechanism may be related to nonhydrostatic effects due to irreversible heat associated with breaking acoustic GWs (Deng & Ridley, 2012). Despite this potential caveat, the hydrostatic approximation is used in this study in that most of whole-atmosphere or thermosphere-ionosphere global models are still based on hydrostatic global circulation models that have been used for the lower atmosphere (see Akmaev, 2011; Schunk, 2012).

4. Dynamically Balanced Flow

4.1. Initialization of Dynamical Model and Physics Forcing

The dynamical model described above needs to be initialized to generate balanced flow at specific date and time. Global distributions of the horizontal winds, temperature, and three tracers (the specific humidity and specific contents of liquid cloud and cloud ice) can be obtained from G2S profiles described in section 2. Apart from these variables, the model needs the surface pressure for initialization. The surface pressure (p_s) is required to initially define the pressure on the η surfaces. Initial p_s at specific date and time is obtained from the ERA-Interim data. However, the p_s taken from the ERA-Interim is generally incompatible with our dynamical model because the model's topographic heights, the same as in the Community Atmosphere Model, and G2S temperature and humidity profiles would not be consistent with the p_s of the ERA-Interim. Hence, the p_s from the ERA-Interim is corrected considering difference between model's topography and ERA-Interim topography and using the post process as in Haseler and Sakellarides (1986).

As shown in (1) and (2), appropriate physics forcing terms at specific date and time are necessary to drive the dynamical model. Global distributions of physics forcing terms are specified using 30-year averaged values of various instantaneous physics forcing terms archived every 6 hr in a climatological experiment carried out specified chemistry version of National Center for Atmospheric Research Whole Atmosphere Community Climate Model (SC-WACCM; K. L. Smith et al., 2014) at the default WACCM resolution (66 layers and 1.9° latitude × 2.5° longitude). That is, physics forcing terms used in (1) and (2) represent SC-WACCM climatological physics terms at a specific instant of time (00, 06, 12, or 18 UT) on one of 365 days. Physics forcing term for momentum ($\boldsymbol{P_u}$) includes the three parameterized GW momentum forcing terms due to orography, convection, and frontal systems, viscosity due to vertical diffusion, and ion drag. Physics forcing terms for temperature (P_T) include convective adjustment heating, total shortwave heating (solar radiation, extreme ultraviolet [EUV] heating,

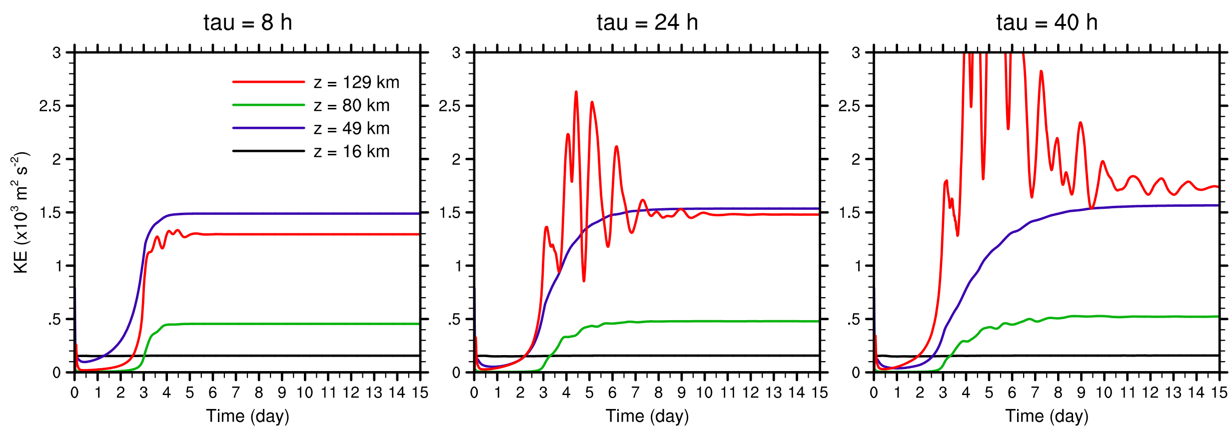

Figure 3. Time series of globally averaged horizontal kinetic energies given by $(u^2 + v^2)/2$ at the altitudes of (black) 16, (blue) 49, (green) 80, and (red) 129 km for the nudging time scale τ of (left) 8, (center) 24, and (right) 40 hr at 0000 UT on 1 July 2014. KE = kinetic energy.

chemical potential heating, CO_2 near-infrared heating, auroral heating, and non-EUV photolysis term), total longwave heating (Earth's radiation and nonlocal thermodynamic equilibrium terms related to CO_2 and NO), GW-induced heating, and vertical thermal diffusion.

4.2. Generation of Balanced Flow

Balanced flow is generated by iteratively nudging the dynamical model forced by physics forcing terms toward G2S data at specific date and time until the model approaches a nominal steady state. During the iteration, evolutions of the model variables are constrained by the assimilation terms [(1) and (2)] associated with the G2S data at the same specific time. The assimilation terms are essential for balanced flow to be valid at a specific date and time, and they are given by

$$\boldsymbol{A_u} = -\frac{\boldsymbol{u} - \boldsymbol{u}_{\mathrm{G2S}}}{\tau} - \frac{\partial \boldsymbol{u}_{\mathrm{G2S}}}{\partial t}, \tag{5}$$

$$\text{and } A_T = -\frac{T - T_{\mathrm{G2S}}}{\tau} - \frac{\partial T_{\mathrm{G2S}}}{\partial t}, \tag{6}$$

where τ is the nudging time scale, and the local time changes of G2S winds and temperature are precomputed through the centered differentiation of the two additionally computed G2S data at $\pm$5 min around a specific time (00, 06, 12, or 18 UT). To compute the two additional G2S data, the 6-hourly ERA-Interim and MERRA data are linearly interpolated in time, but the empirical models for the upper atmosphere are computed exactly at $\pm$5 min around the specific time, which may help in better representing time variations of the atmospheric tides in the upper atmosphere.

Although the model is run until it reaches a nominal steady state to obtain a balanced flow, balanced flow itself is not necessarily in a real steady state. Balanced flow should be defined as being time dependent, as discussed by McIntyre (2015a). Therefore, in this study, balanced flow is generated so that it can represent slowly varying properties of the large-scale flow by including the local time changes taken from G2S profiles (i.e., $-\partial \boldsymbol{u}_{\mathrm{G2S}}/\partial t$ and $-\partial T_{\mathrm{G2S}}/\partial t$) in the assimilation terms. When the model finally approaches a nominal steady state, the local time changes of model variables become zero in (1) and (2) (i.e., $\partial \boldsymbol{u}/\partial t = \partial T/\partial t = 0$). For balanced flow in a nominal steady state, however, it is reasonable to state that the local time changes of winds and temperature are actually given by the G2S local time changes ($\partial \boldsymbol{u}_{\mathrm{G2S}}/\partial t$ and $\partial T_{\mathrm{G2S}}/\partial t$) in the assimilation terms, given that (1) and (2) can be written by $\partial \boldsymbol{u}_{\mathrm{G2S}}/\partial t + \cdots = \boldsymbol{P_u} - (\boldsymbol{u} - \boldsymbol{u}_{\mathrm{G2S}})/\tau$, and $\partial T_{\mathrm{G2S}}/\partial t + \cdots = \boldsymbol{P}_T - (T - T_{\mathrm{G2S}})/\tau$, respectively, in a nominal steady state.

In balanced flow generated in this study, the local time change of the pressure depth in (3) (i.e., $\partial/\partial t\,(\partial p/\partial \eta)$) actually becomes 0, and as a result the surface pressure (obtained by integrating $\partial/\partial t\,(\partial p/\partial \eta)$ from model top to the surface) does not vary with time either. Note that there is no assimilation term for the local time changes of the pressure depth in (3). The fact that the local time changes of the pressure at each layer and at the surface are actually 0 in a balanced flow indicates that high-frequency waves due to pressure fluctuations would not be induced when the balanced flow is used as a model initial condition. It is also noticeable that, if $\partial/\partial t(\partial p/\partial \eta) = 0$ and if $\partial p/\partial \eta$ can be assumed to be a quantity related to air density (pseudo air density), (3) is reduced to the mass continuity equation in soundproof systems such as the anelastic or pseudo-incompressible air-flow systems (see Durran, 1989, 2008; Lipps & Hemler, 1982; Smolarkiewicz et al., 2014). If the G2S local time changes are not considered in the assimilation terms (i.e., $\partial \boldsymbol{u}_{\mathrm{G2S}}/\partial t = 0$, and $\partial T_{\mathrm{G2S}}/\partial t = 0$), balanced flow actually approaches a steady state. In our results, G2S local time change terms are included unless otherwise stated, but when the time change terms are neglected, realism of balanced flow is diminished, which will be discussed later. In either case (zero or nonzero G2S tendencies), the nudging terms in a nominal steady state represent deviations of balanced flow from G2S data.

As the iteration proceeds, global distributions of tracers evolve, and thus they gradually become different from those given at specific date and time. To prevent this unwanted evolution, the tracer variables are replaced with the values given as initial conditions of the model at specific date and time after every physics time step. To minimize destabilizing effects of initial spurious waves, Rayleigh damping for winds and temperature is applied for an initial 1 day. Rayleigh damping coefficients are specified so that they are almost 0 below 1 hPa, increase with height above 1 hPa, and remain constant in the lower thermosphere and above. The damping gradually decreases in time and eventually disappears after 1 day (see Figure S1 in the supporting information).

Figure 3 shows time series of globally averaged horizontal kinetic energies (KEs) at the altitudes of 16, 49, 80, and 129 km for three different values (8, 24, and 40 hr) of τ at 0000 UT on 1 July 2014. For initial 1–2 hr, KEs above $z = 49$ km remain substantially small due to the initial Rayleigh damping, but after 1–2 hr they gradually increase. It is clearly seen in Figure 3 that results of the dynamical model depend on the nudging time scale (τ) in (5) and (6). The global mean KE at each level approaches a constant value in 15 days for $\tau \leq 40$ hr as the model approaches a nominal steady state. For a small (large) value of τ, it takes short (long) time for the model to approach its nominal steady state because the model is strongly (weakly) constrained by G2S profiles. As τ increases, the KE rapidly oscillates in the lower thermosphere, which implies that the atmospheric flows above the mesopause (initially specified by the empirical models) are far from dynamical balance, and it may also severely be affected by amplification of spurious initial waves generated in the lower atmosphere. The global-mean KEs in nominal steady states depend on the values of τ and roughly increase with τ above $z = 49$ km. In other words, the model can reach its own nominal steady state for any τs, which indicates that there should be constraints to choose an appropriate value for τ.

4.3. Determination of Nudging Time Scale

For the tropospheric NWP, nudging coefficients (τ^{-1}s) have been chosen as 10^{-5}–10^{-4} s^{-1} through experiences (e.g., Hoke & Anthes, 1977; Krishnamurti et al., 1991) at horizontal resolution finer than 1° or determined as 10^{-4}–10^{-3} s^{-1} through variational approaches (e.g., Zou et al., 1992) at about 2° resolution. As discussed by Zou et al. (1992), nudging coefficient may tend to increase with decreasing horizontal resolution. In this regard, the values of 10^{-5}–10^{-4} s^{-1} might be better choices for our dynamical model with about 1° resolution. However, these values were used in the tropospheric NWP models, and it is not clear that they would work in the upper atmosphere. Besides, criteria to choose the values have not been clearly presented. For these reasons, in this study, we attempt to determine the nudging coefficient based on physically based criteria.

To determine nudging time scale in a physically based way, we estimate GW momentum forcing and residual mean meridional circulations from balanced flow and then examine dependence of their structure on τ. Liu et al. (2009) demonstrated that GW momentum forcing in the MLT region in WACCM can be, to a substantial degree of accuracy, represented by the sum of the Coriolis term, curvature term, and a term related to meridional advection and eddy transport. This result implies that the atmospheric flow in the MLT region is in a state where GW momentum forcing is balanced by the sum of those terms. Following the formulation in Liu et al. (2009), the zonally averaged zonal GW momentum forcing ($\bar{F}_{\lambda}^{\mathrm{GW}}$) is estimated as follows:

$$\bar{F}_{\lambda}^{\mathrm{GW}} = -\left(f + \frac{\bar{u}\tan\phi}{a}\right)\bar{v} + \overline{\frac{v}{a}\frac{\partial u}{\partial \phi}}, \tag{7}$$

where $\bar{u}$ and $\bar{v}$ are the zonal-mean zonal and meridional winds, respectively; a is the mean radius of the Earth; and the overbar denotes zonal averaging.

The residual mean meridional circulation obtained in the transformed Eulerian-mean system represents the Lagrangian mass circulation in the stratosphere and MLT region where the large-scale atmospheric flow is predominantly driven by atmospheric waves (Andrews et al., 1987; A. K. Smith, 2012). Atmospheric waves can

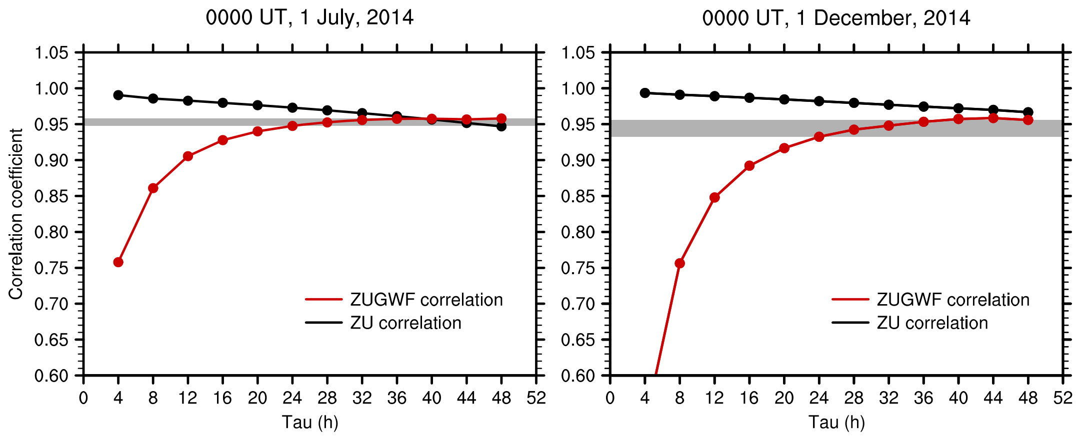

Figure 4. Correlation coefficients (red) between zonal-mean zonal GW momentum forcing estimated from the balanced flow and SC-WACCM climatological GW momentum forcing and (black) between zonal-mean zonal wind in the balanced flow and G2S zonal wind as a function of τs from 4 to 48 hr for (left) 0000 UT on 1 July 2014 and (right) 0000 UT on 1 December 2014. For the balanced flow, results at 15 days are used. Correlation coefficients are computed over all the latitudes and the height range between 50 and 110 km. Gray shading denotes the range of the correlation coefficients for the GW forcing for $24 \leq \tau \leq 48$ hr. GW = gravity wave; SC-WACCM = specified chemistry version of the Whole Atmosphere Community Climate Model; G2S = ground-to-space; ZUGWF = Zonal-mean zonal GW momentum forcing.

induce the mean vertical motion called the Stokes drift as they propagate vertically in a steady and conservative manner (Dunkerton, 1978). The residual mean meridional circulation ($\bar{v}^*$, $\bar{w}^*$) represents effects of the Stokes drift, and it is computed using the formulations in the log-pressure coordinate (z) (Andrews et al., 1987) given by

$$\bar{v}^* = \bar{v} - \frac{1}{\rho_0}\frac{\partial}{\partial z}\left(\frac{\rho_0 \overline{v'\theta'}}{\partial\bar{\theta}/\partial z}\right), \tag{8}$$

$$\text{and } \bar{w}^* = \bar{w} + \frac{1}{a\cos\phi}\frac{\partial}{\partial\phi}\left(\frac{\overline{v'\theta'}\cos\phi}{\partial\bar{\theta}/\partial z}\right), \tag{9}$$

where $\bar{\theta}$ is the zonal-mean potential temperature, ρ_0 is the air density given by $\rho_s e^{-z/H}$, ρ_s is the air density at $z = 0$, H is the scale height (= 7 km), and v' and θ' are wave-induced perturbations for meridional wind and potential temperature, respectively.

Figure 4 shows correlation (Pearson product-moment) coefficients in the MLT region between the zonal-mean zonal GW momentum forcing estimated from balanced flow and SC-WACCM climatological GW forcing and between the zonal-mean zonal wind obtained from balanced flow and the zonal-mean G2S zonal wind. Correlation coefficients are given as a function of τs ranging from 4 to 48 hr at 0000 UT on 1 July 2014 and 1 December 2014. For balanced flow, results at 15 days are used. From Figure 4, it is clear that the correlation coefficient for GW momentum forcing increases with τ and becomes saturated at about 0.94–0.96 for $\tau \geq 36$ hr, whereas correlation coefficient for zonal wind almost linearly decreases with τ. As τ increases, the dynamical model is less constrained by G2S profiles, and as a result estimated GW momentum forcing approaches the climatological GW forcing that may not be expected to represent a structure of GW momentum forcing at specific date and time. Meanwhile, the zonal-mean zonal wind of balanced flow becomes different from G2S zonal wind as τ increases. This result indicates that an appropriate value of τ can be determined somewhere in the middle of the range of τs shown in Figure 4 so that balanced wind may not be too much different from G2S wind, and GW momentum forcing estimated from balanced flow may not be too much similar to the climatological GW forcing. Correlation coefficients for equinox seasons (Figure S2) also support this result for the solstice seasons: An optimal value of τ should be chosen in the middle of τs (4–48 hr).

Figure 5 shows latitude-height cross sections of zonal-mean zonal GW momentum forcing from the SC-WACCM climatology and from balanced flows generated using three different τs at 0000 UT on 1 July 2014 and 1 December 2014. The SC-WACCM climatology exhibits a typical structure of GW momentum forcing, westward (eastward) acceleration in the winter (summer) hemisphere, required to reasonably simulate wind and temperature climatologies in the MLT region. This structure of GW forcing is qualitatively similar to that

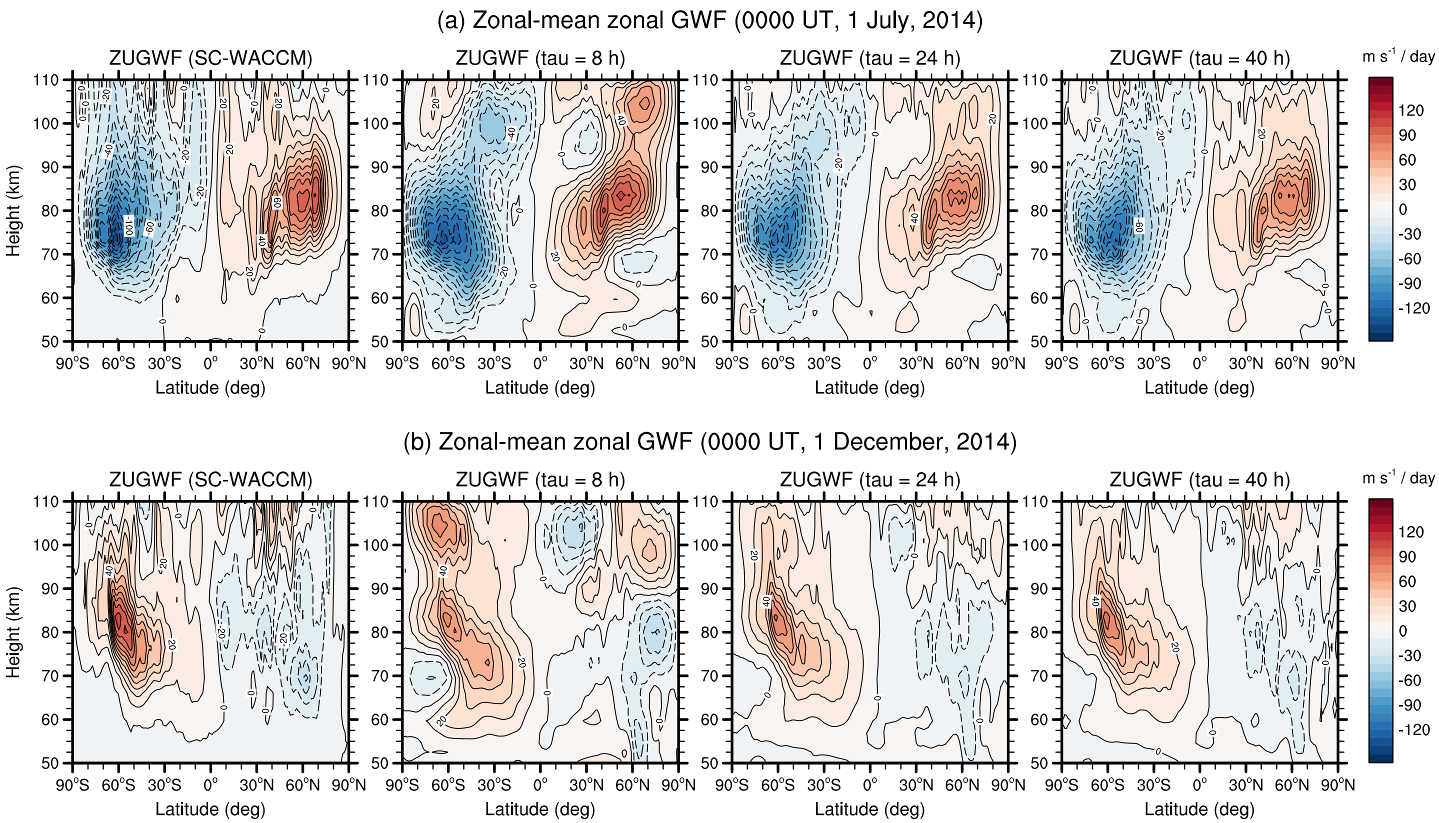

Figure 5. Latitude-height cross sections of the zonal-mean zonal GW momentum forcing from the SC-WACCM climatology and from the balanced flows generated using $\tau = 8$, 24, and 40 hr at (a) 0000 UT on 1 July 2014 and at (b) 0000 UT on 1 December 2014. Contour interval is 10 m$\cdot$s$^{-1}\cdot$day^{-1}, and negative values are plotted in dashed lines. GW = gravity wave; SC-WACCM = specified chemistry version of the Whole Atmosphere Community Climate Model; ZUGWF = Zonal-mean zonal GW momentum forcing.

in the other whole atmospheric models (see A. K. Smith, 2012, for the list of the high-top models). When τ is small (8 hr), comparison with the climatology shows that estimated GW forcing exhibits quite a different latitudinal structure in the lower thermosphere ($z > 95$ km) and is substantially enhanced in the lower mesosphere ($z < 60$ km). The structure of GW forcing becomes similar to that of the climatology as τ increases, as expected from Figure 4, but around $\tau = 24$ hr, GW forcing does not approach completely the climatology. Estimated GW forcing when $\tau = 24$ hr exhibits distinctive structure compared with the climatology: Westward GW forcing of 10–20 m$\cdot$s$^{-1}\cdot$day^{-1} appears from $z = 50$–60 km in winter, eastward GW forcing is extended toward the equator from the middle of the summer mesosphere, westward GW forcing in the high-latitude upper mesosphere in winter is extended toward the midlatitude lower thermosphere, and eastward GW forcing of 20–30 m$\cdot$s$^{-1}\cdot$day^{-1} is vertically stretched toward the lower thermosphere in summer. This distinctive structure is more clearly seen in time-averaged forcing (Figure S4). When $\tau = 40$ hr, estimated GW forcing looks more similar to the climatology and becomes spatially localized as in the climatology. In equinox seasons, τ of 24 hr also yields appropriate structure of GW forcing between the climatology and structure severely constrained by G2S data for $\tau = 8$ hr (Figure S5). The magnitude of GW forcing is overall small in equinox seasons, but a characteristic structure of estimated GW forcing such as enhanced (reduced) GW forcing in the lower (middle) mesosphere when compared to the climatology is also found for $\tau = 24$ hr as in the solstice seasons.

GW momentum forcing shown in Figure 5 is estimated by including the local time change terms in the assimilation terms in (5) and (6). Without the local time change terms, GW forcing in the mesosphere becomes more vertically localized as in the climatology (see Figure S3). Therefore, the spatially diffused structure of GW momentum forcing estimated in the lower mesosphere when $\tau = 24$ hr seems to be partially due to the local time change of the large-scale flow. In Figure 5, when compared with the climatology, reduction of westward GW forcing estimated using $\tau = 24$ hr in the high-latitude winter midmesosphere may help alleviate common model biases that wind reversals in the mesosphere appear at the lower altitudes than observations due to large GW forcing localized in the midmesosphere (see, e.g., Figure 2 in A. K. ; Smith, 2012). GW momentum

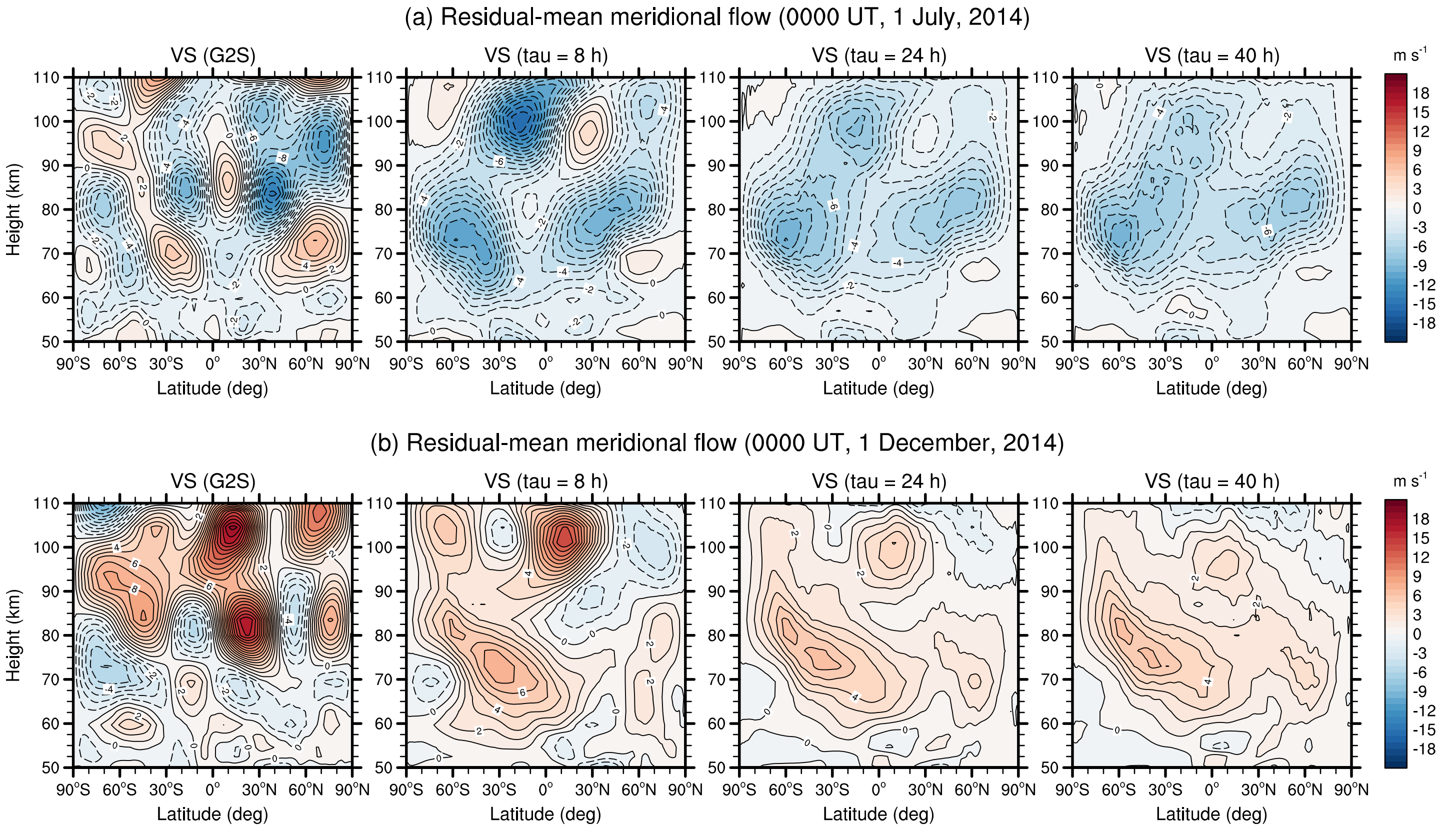

Figure 6. Latitude-height cross sections of the residual mean meridional flows from the G2S data and from the balanced flows generated using τ = 8, 24, and 40 hr at (a) 0000 UT on 1 July 2014 and at (b) 0000 UT on 1 December 2014. Contour interval is 1 m/s, and negative values are plotted in dashed lines. G2S = ground-to-space; VS = Residual-mean meridional flow.

forcing in models needs to be overall corrected such that it can produce the more (less) westward GW forcing in the midlatitude upper mesosphere (in the high-latitude midmesosphere) for the better simulation for the MLT region in winter. This correction suggestion may be supported by modeling studies on chemical transport (e.g., McLandress et al., 2013; Meraner et al., 2016). The modeling studies have pointed out that enhanced (reduced) westward GW forcing in the upper mesosphere (midmesosphere) in winter allows for more realistic downward transport of chemicals from the lower thermosphere.

Figure 6 shows latitude-height cross sections of the residual mean meridional flow obtained from G2S profiles and from balanced flows generated using three different τs at 0000 UT on 1 July 2014 and 1 December 2014. The residual mean meridional flow estimated from G2S profiles does not exhibit the one-cell circulation with the summer-to-winter flow in the upper mesosphere at all. That is, G2S profiles in the upper atmosphere, mainly specified using the empirical models, do not represent properly the atmospheric dynamics in the MLT region. Meanwhile, balanced flow generated using physics forcing terms and assimilation terms can reasonably represent the pole-to-pole flow in the MLT region. When τ is small (8 hr), however, the meridional flow exhibits a complicated latitudinal structure in the mesosphere that does not clearly represent the pole-to-pole meridional flow. As τ increases, the summer-to-winter meridional flow becomes dominant in the middle to upper mesosphere. When $\tau = 24$ hr, there is a substantial meridional flow near the equatorial mesopause region, but when $\tau = 40$ hr, this upper mesospheric meridional flow becomes weak, and the meridional flow becomes overall confined in the midmesosphere. As shown in Figure 4, estimated GW forcing is substantially close to the climatology when $\tau = 40$ hr. Therefore, the meridional flow in the midmesosphere at $\tau = 40$ hr seems to be more related to the climatological GW forcing that produces the mesopause at the lower altitudes than observations. In time-averaged residual mean meridional circulations (Figure S4), it is more clearly seen that the summer-to-winter meridional flow occurs throughout the middle to upper mesosphere when $\tau = 24$ hr, and compensating upward and downward motions appear in the polar mesosphere. In equinox seasons, the residual circulations are weak, and they do not exhibit a characteristic structure as in the solstice

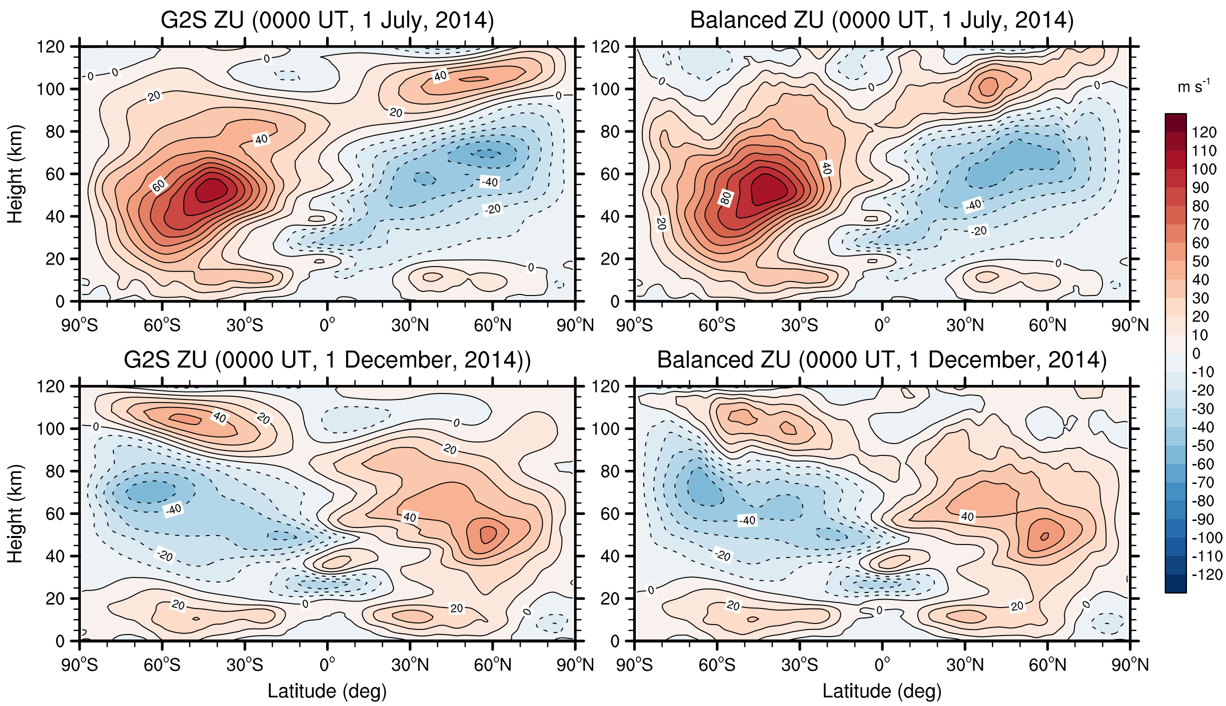

Figure 7. Latitude-height cross sections of the zonal-mean zonal wind from the G2S data and from the balanced flow generated using τ = 24 hr at (top) 0000 UT on 1 July 2014, and at (bottom) 0000 UT on 1 December 2014. Contour interval is 10 m/s, and negative values are plotted in dashed lines. G2S = ground-to-space; ZU = Zonal-mean zonal wind.

seasons (Figure S6). However, it seems clear that τ of 24 hr gives a structure of the residual mean meridional flow between the climatological structure and a complicated structure induced by strong nudging toward the G2S data.

4.4. Structure of Balanced Flow

In the previous subsection, it is shown that the nudging time scale τ of about 24 hr ($\tau^{-1} \approx 1.16\times10^{-5}$ s^{-1}) may produce reasonable structure of GW momentum forcing and residual mean meridional circulation. This structure is not identical to the climatological structure to be induced by physics forcing terms. This disagreement can make us expect balanced flow generated with τ = 24 hr to somehow represent particularities of the whole atmosphere at specific date and time.

Figure 7 shows the zonal-mean zonal wind from G2S profiles and balanced flow generated using τ = 24 hr at 0000 UT on 1 July 2014 and 1 December 2014. Balanced flow reasonably represents typical structure of the zonal-mean zonal wind from the troposphere to the lower thermosphere as in G2S profiles: tropospheric subtropical jets, equatorward tilted polar night jet in the stratosphere and the lower mesosphere in winter, wind reversals near the mesopausal region, and the higher (lower) mesopause height in winter (summer). Zonal-mean temperature in balanced flow also reasonably exhibits the whole atmospheric thermal structure (not shown). Even though τ is determined based on the MLT dynamics, the zonal-mean zonal wind in balanced flow appropriately reproduces G2S zonal wind in the troposphere and stratosphere as well. G2S profiles below the stratopause are mainly determined by the meteorological analyses that are significantly constrained by observations at specific date and time. Therefore, similarity between balanced flow and G2S profiles below the stratopause indicates that balanced flow generated using τ = 24 hr can realistically represent the atmospheric flow at specific date and time. In the MLT region, balanced flow exhibits substantial differences from G2S data in some places. The midmesospheric polar night jet in balanced flow exhibits larger latitudinal variations. The structure of the westward jet in the summer mesosphere is changed in balanced flow. In the summer lower thermosphere, the eastward jet cores are located at different latitudes in balanced flow.

Figure 8 shows the Eliassen-Palm (EP) flux vectors obtained from G2S profiles and balanced flow generated using τ = 24 hr at 0000 UT on 1 July 2014 and 1 December 2014. The magnitudes of the meridional and vertical components of the EP fluxes are proportional to the group velocities (meridional and vertical components)

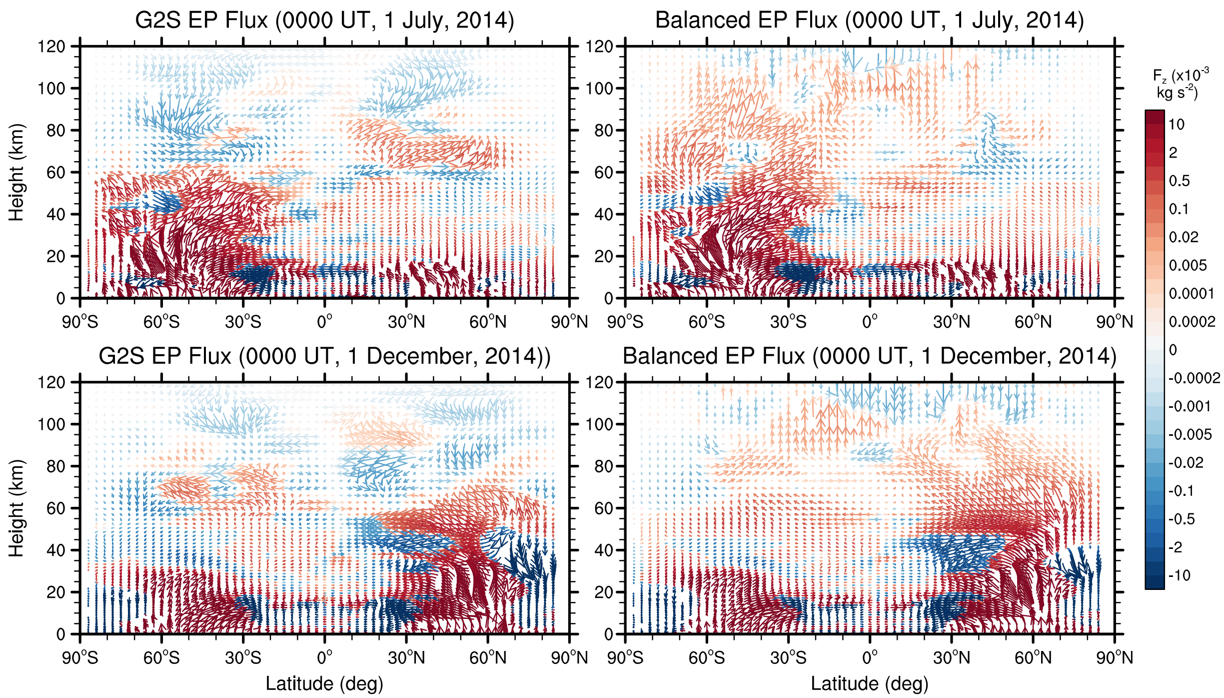

Figure 8. Latitude-height cross sections of the EP flux vector fields obtained from the G2S data and from the balanced flow generated using τ = 24 hr at (top) 0000 UT on 1 July 2014 and (bottom) 0000 UT on 1 December 2014. For better illustration of the directions of EP flux vectors in the latitude and height ranges of 90°S–90°N and 0–120 km, the meridional components of the EP flux vectors are reduced by a factor of 120 km/($a\pi$) km, where a is the mean radius of the Earth, and $a\pi$ denotes the distance along a meridian between the two poles. Then, the EP flux vectors at each vertical level are normalized by the global-mean value of the EP flux magnitudes at the same level. Colors of the vectors indicate the vertical components of the EP fluxes. Color interval is logarithmic in the range of $\pm 10 \times 10^3$ kg/s^2. EP = Eliassen-Palm; G2S = ground-to-space.

and activity density of the large-scale atmospheric waves. The EP fluxes are computed following Andrews et al. (1987) using the formulations given by

$$F_\phi = \rho_0 a \cos\phi \left(\frac{\partial \bar{u}}{\partial z} \frac{\overline{v'\theta'}}{\partial \bar{\theta}/\partial z} - \overline{v'u'} \right), \tag{10}$$

$$\text{and } F_z = \rho_0 a \cos\phi \left\{ \left[f - \frac{1}{a\cos\phi} \frac{\partial}{\partial \phi} (\bar{u}\cos\phi) \right] \frac{\overline{v'\theta'}}{\partial \bar{\theta}/\partial z} - \overline{w'u'} \right\}, \tag{11}$$

where F_ϕ and F_z are the meridional and vertical components of EP flux, respectively; w' is the perturbation vertical velocity in the log-pressure coordinate and approximately computed using the relation $w' \approx -H\omega'/p$ where ω' is the perturbation pressure velocity.

As is expected, in G2S data, vertical discontinuities of the EP flux vectors are found in the winter lower mesosphere (z = 60–80 km), due to spectral discrepancy between the meteorological analysis and empirical models. The structure of the EP fluxes below the midstratosphere ($z \approx 40$ km) is similar between G2S data and balanced flow, but it becomes significantly different above the stratopause. The EP fluxes in balanced flow demonstrate that large-scale waves generated from the winter troposphere can propagate through the eastward jet regions to the mesopause. This result is consistent with the vertical propagation of quasi-stationary waves through the wave guide of the eastward jet (Charney & Drazin, 1961). In balanced flow, this wave guide is extended toward the summer hemisphere across the equator as shown in Figure 7, and quasi-stationary large-scale waves actually propagate within the wave guide crossing the equatorial lower thermosphere. Wave propagation through this cross-equatorial wave guide is more clearly seen in the time-averaged EP fluxes (Figure S4), similar to that shown in A. K. Smith (2003). In the summer hemisphere, waves from the troposphere do not penetrate the lower stratosphere where zonal wind direction changes from eastward to westward. Therefore, it is reasonable to consider those waves from the summer troposphere as being mostly quasi-stationary. Above the stratopause and below the middle mesosphere (z = 50–80 km) in the summer hemisphere, for balanced flow, there seem to be additional wave source regions in the subtropical and midlatitude regions where the EP flux vectors are locally divergent or convergent. In the summer lower mesosphere,

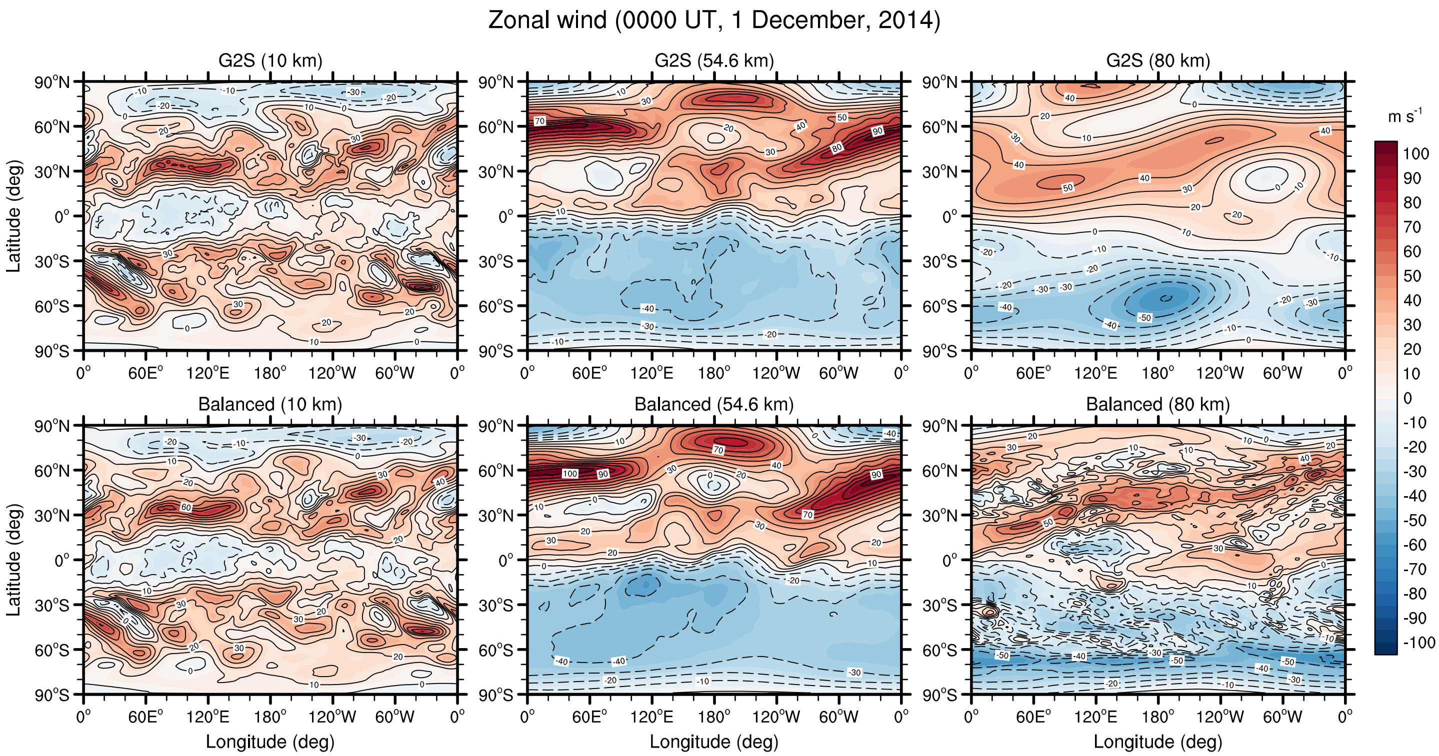

Figure 9. Longitude-latitude distributions of zonal wind at (left) $z = 10$, (middle) $z = 54.6$, and (right) $z = 80$ km from (top) the G2S data and from (bottom) the balanced flow generated using $\tau = 24$ hr for 0000 UT on 1 December 2014. Shading interval is 5 m/s. Contour interval is 10 m/s, and negative values are plotted in dashed lines. G2S = ground-to-space.

the westward jet is predominant as shown in Figure 7, and therefore the large-scale waves excited above the summer stratopause regions are likely to be transient. Near the winter stratopause, locally divergent (or convergent) EP fluxes are found in balanced flow around 50–70°S in July and 70–90°N in December. These regions are found at a specific date and time as shown in Figure 8 but not seen in monthly averaged structure (Figure S4).

As shown in Figure 8, balanced flow in the MLT region is significantly affected by vertically propagating waves generated from the stratosphere and troposphere. The vertical coupling through waves between the MLT region and the lower atmosphere constrained by observations at specific date and time allows for production of balanced flow that is realizable in the MLT region at the same date and time. This rationale can also be found in several whole atmospheric modeling studies. In these studies, reliable atmospheric flows in the MLT region in a particular period of time are expected to be produced by nudging models in time toward series of the atmospheric analysis data below the stratopause or below the upper mesosphere in the same time period (e.g., Brakebusch et al., 2013; Marsh, 2011; Randall et al., 2015; Siskind et al., 2015).

Figure 9 shows longitude-latitude distributions of the zonal wind from G2S data and balanced flow generated using $\tau = 24$ hr at $z = 10$, 54.6, and 80 km at 0000 UT on 1 December 2014. As in the zonal-mean zonal wind (Figure 7), horizontal wind structure in balanced flow below the lower mesosphere ($z = 10$ and 54.6 km) reasonably represents the structure of the G2S wind whose the stratospheric and tropospheric parts are mainly determined by the meteorological analyses. In the troposphere ($z = 10$ km), the subtropical and midlatitude jets in both hemispheres in balanced flow are quite similar to those in G2S data (i.e., similar to jets in the ERA-Interim and MERRA data). Just above the stratopause ($z = 54.6$ km), the structure of the polar night jet in the Northern Hemisphere in G2S data, similar to that in the MERRA data, is almost reproduced in balanced flow. In the Southern Hemisphere, however, the westward jets with somewhat different spatial structure are produced in balanced flow. This difference may be related to different structure of EP fluxes in the summer lower mesosphere (Figure 8). The different EP flux structure can be due to transient large-scale waves in balanced flow in the summer midmesosphere that are either absent or weak in G2S data. In the upper mesosphere ($z = 80$ km), the zonal wind in balanced flow shows a large-scale structure of the polar night jet

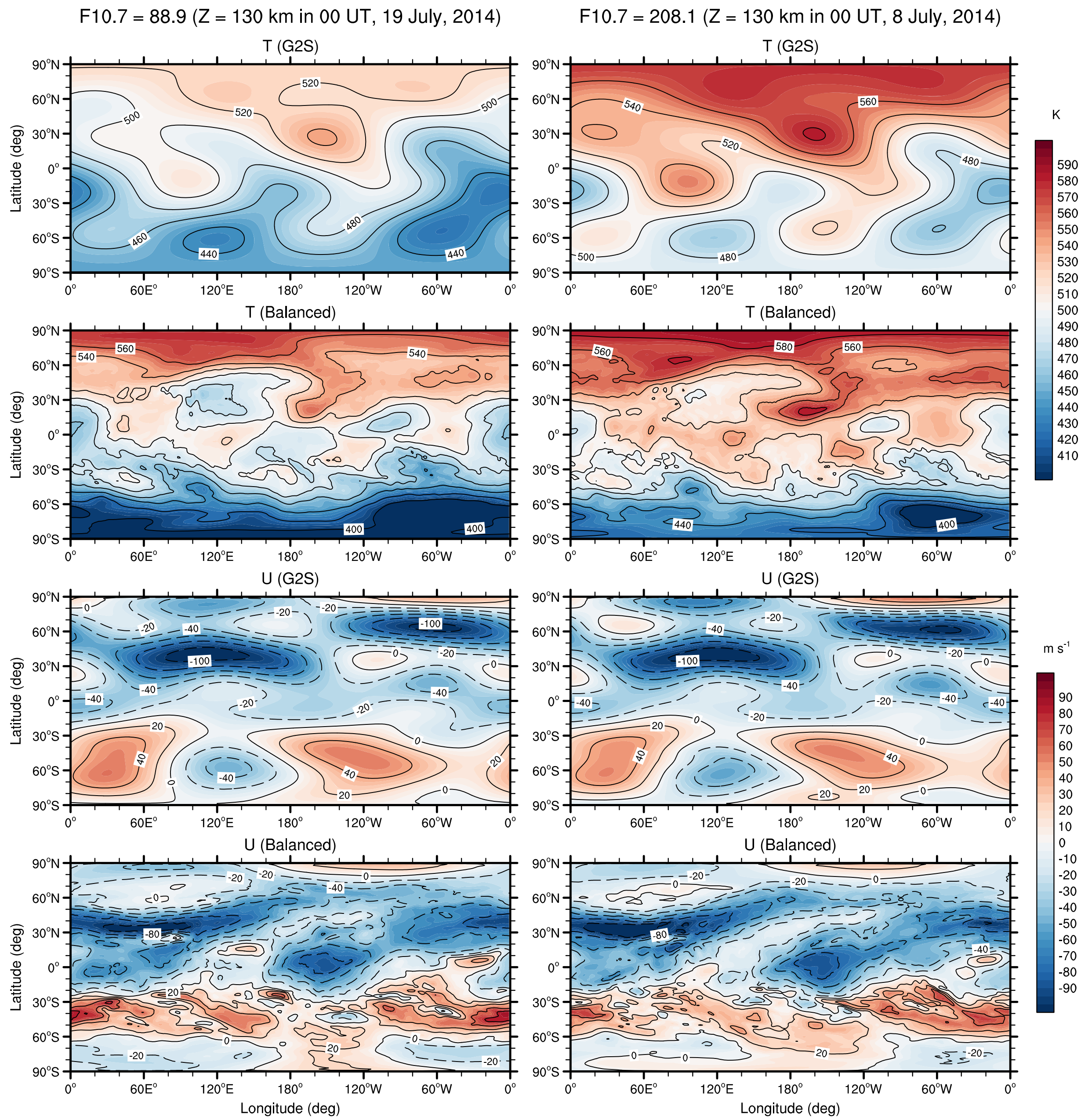

Figure 10. Longitude-latitude distributions of temperature and zonal wind in the G2S data and balanced flow at the altitude of about 130 km (9.83×10^{-6} hPa) at 0000 UT on (left column) 19 July 2014 when solar activity is minimum in July 2014 ($F_{10.7}$ = 88.9 in solar flux units [sfu]) and on (right column) 8 July 2014 when solar activity is maximum in July 2014 ($F_{10.7}$ = 208.1 sfu). Shading intervals for zonal wind and temperature are 5 m/s and 5 K, respectively. Contour intervals for zonal wind and temperature are 20 m/s and 20 K, respectively, and negative values are plotted in dashed lines. G2S = ground-to-space.

and planetary waves as shown in G2S data and a small-scale structure that seems related to the large-scale instability. This instability is further discussed in the next section.

Figure 10 shows longitude-latitude distributions of temperature and zonal wind in the lower thermosphere for G2S and balanced flow at the altitude of about 130 km (9.83 × 10^{-6} hPa) at 0000 UT on 19 July 2014 when solar activity is minimum in July 2014 and on 8 July 2014 when solar activity is maximum in the same month. Time variations of solar activity were substantial in July and December 2014. Here solar activity is denoted by the $F_{10.7}$ index, the 10.7 cm solar radio flux expressed in solar flux units, where 1 sfu = 10^{-22} W·m^{-2}·Hz^{-1}. Minimum and maximum values of $F_{10.7}$ were 88.9 and 208.1 sfu in July and 125.0 and 208.9 sfu in December, respectively. These variations of $F_{10.7}$ almost correspond to monthly variations of $F_{10.7}$ found in the 11-year

10.1029/2017MS001213

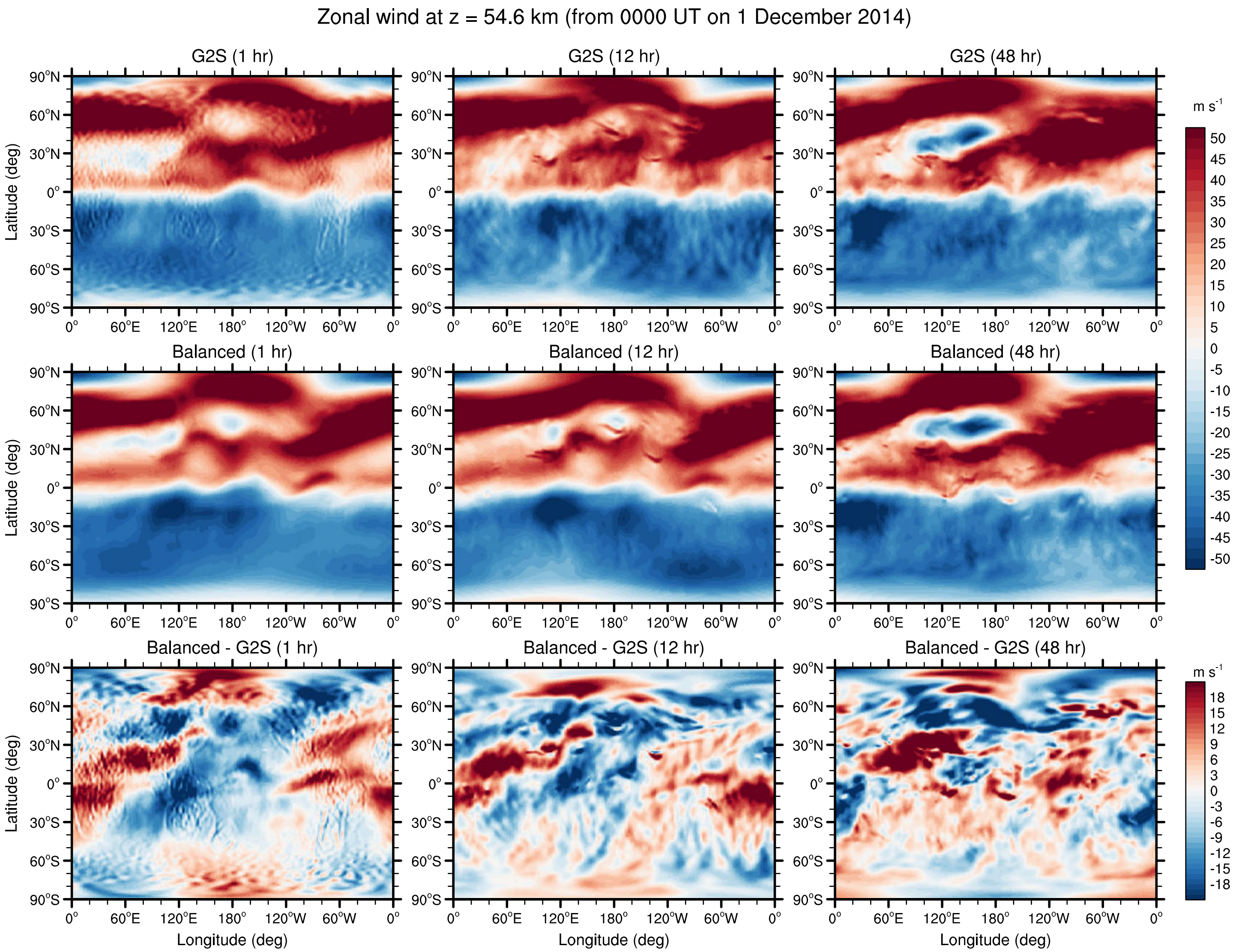

Figure 11. Time evolution of the horizontal distributions of the zonal wind at z = 54.6 km in forecast runs carried out using the SC-WACCM (with full physics) initialized with (top row) unbalanced and (middle row) balanced flows at 0000 UT on 1 December 2014 and (bottom row) their difference in (left) 1-hr, (middle) 12-hr, and (right) 48-hr forecasts. Shading intervals for the zonal wind and its difference are 2.5 and 1 m/s, respectively. SC-WACCM = specified chemistry version of the Whole Atmosphere Community Climate Model; G2S = ground-to-space.

solar cycles (see Tapping, 2013). First of all, it is clearly seen that temperature and winds in the lower thermosphere depend significantly on local time. This result shows that the lower thermospheric structure, basically determined by the empirical models, is substantially affected by the atmospheric tides. Hence, the horizontal structure of temperature and zonal wind at 00 UT looks quite similar between 8 July and 19 July despite substantial difference in dates. In fact, spectral analysis shows that substantial diurnal and semidiurnal signals in the horizontal winds are found in both G2S and balanced flow (see Figure S7).

In Figure 10, it is found that strong solar activity overall increases temperature in the lower thermosphere, when compared to the date of minimum solar activity, for both G2S and balanced flows (see the first two rows in Figure 10). Horizontal temperature structure in G2S data, however, is quite different from that in balanced flow, which is attributed to thermal physics forcing in the lower thermosphere used to generate balanced flow (not shown). Figure 10 also shows that horizontal wind structure in balanced flow seems to be insensitive to solar activity. This result may be understood in view of the geostrophic balance, given that temperature fields with similar horizontal structure yields similar horizontal wind fields. In December 2014, the lowest and highest solar activities occurred on 6 December and 19 December, respectively. Variation of solar activity is

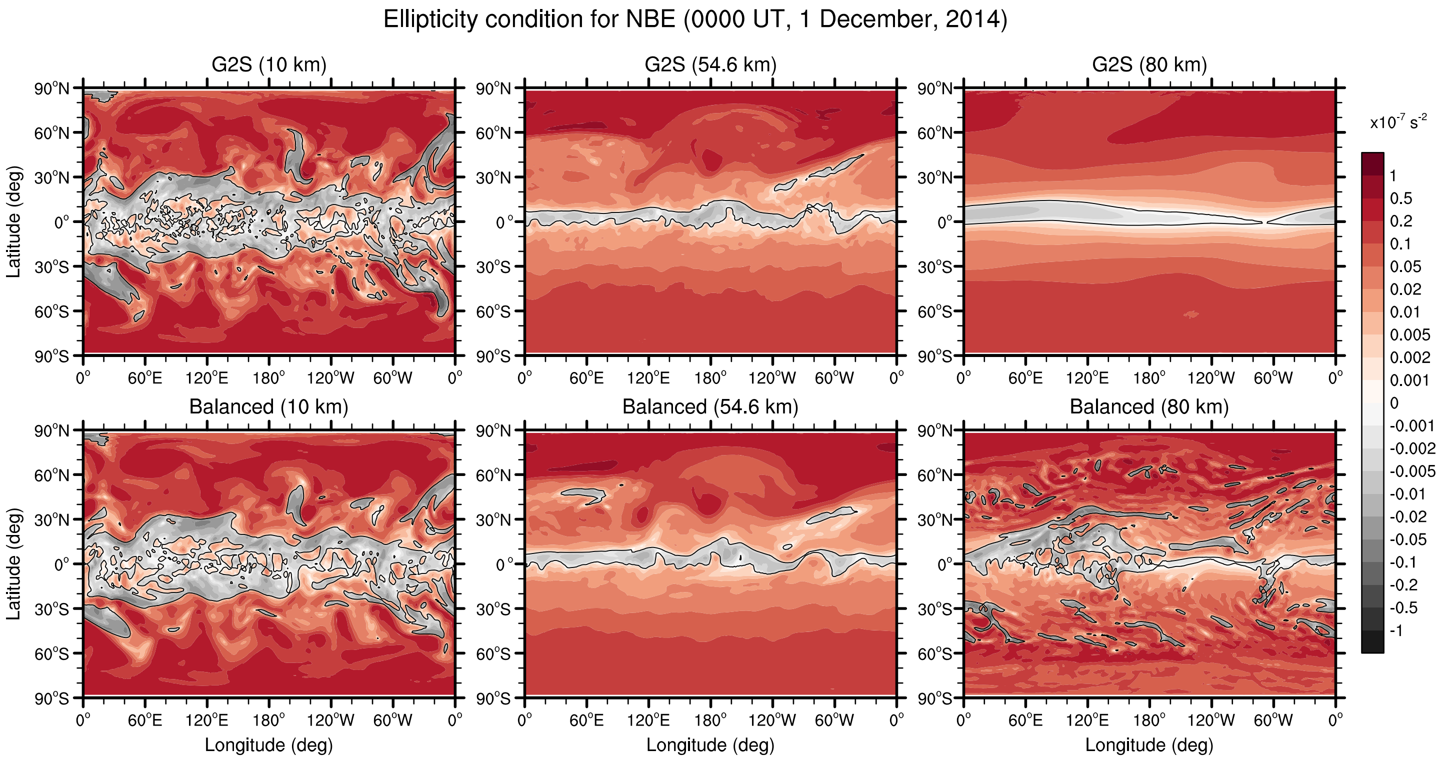

Figure 12. Longitude-latitude distributions of the ellipticity condition of the NBE at (left column) $z = 10$, (middle column) $z = 54.6$, and (right column) $z = 80$ km from (top row) the G2S data and (bottom row) balanced flow generated using $\tau = 24$ hr for 0000 UT on 1 December 2014. Shading interval is logarithmic in the range of $\pm 1 \times 10^{-7}$ s^{-2}, zero line is plotted in black solid line, and negative values are shaded in gray. NBE = nonlinear balance equation; G2S = ground-to-space.

also large in December, but effects of solar activity on the horizontal structure of zonal wind are not significant as in July (Figure S8). Results in Figures 10 and S8 indicate the insensitivity of the balanced horizontal winds in the lower thermosphere on solar activity. However, considering that the HWM14 and physics forcing used in this study do not depend on solar flux, and the number of samples is limited, it is not appropriate to conclude that the insensitivity is actually reliable. More physically based and statistically robust examinations would be necessary in a continuing research.

Figure 11 shows longitude-latitude distributions of the zonal wind and their difference at $z = 54.6$ km at $t = 1$, 12, and 48 hr in forecast runs carried out using the SC-WACCM (with full physics) initialized with G2S data and balanced flow generated using $\tau = 24$ hr at 0000 UT on 1 December 2014. In the SC-WACCM, the same dynamical core as in the dynamical model is employed, and therefore the SC-WACCM is dynamically consistent with the model used to generate balanced flow. The forecast runs are unconstrained by the analysis or G2S data. That is, the SC-WACCM model used in these runs includes neither the climatological physics forcing terms nor assimilation terms in (1) and (2). For these forecast runs, 5-day simulations are carried out. Sea surface temperature (SST) and sea ice fractions are specified using the weekly NOAA Optimum Interpolation SST version 2 data (Reynolds et al., 2002) interpolated in time at 0000 UT on 1 December 2014. For ozone, climatological data are used. The $F_{10.7}$ and Ap indices are specified using values averaged for the 5-day forecast period. Model physics is computed every 15 min. When balanced flow is used as an initial condition, Rayleigh damping is not used, and dynamical time step size of 22.5 s is employed as in the dynamical model. When the model is initialized with G2S data, however, Rayleigh damping and strong second-order viscosity are used throughout the forecast time period above the mesopause (see the right panel of Figure S1) to damp high-frequency waves amplifying near the model top, and dynamic time step size is 10 times reduced for numerical stability (i.e., $\delta t = 2.25$ s).

When the SC-WACCM is initialized using G2S data, the zonal wind shows substantially noisy patterns. Most of noise patterns in the 1-hr forecast seem to be propagated from the lower atmosphere because the noise patterns initially resemble geographical boundary structure. Large noises found over the Southern Ocean seem to be induced along the boundaries of the Antarctica. Weak noises are also found near the surface in the 1-hr forecast (compare 1,012.5-hPa contours of the surface pressure over the oceans between G2S and balanced flow in Figure S9). In the 1-hr forecast, those noise patterns with small horizontal scales in the zonal wind are conspicuous in smooth large-scale structure. In the 12-hr forecast, they are spatially diffused and seem to modify the large-scale structure of dynamical variables. Initial noisy patterns are nearly diminished after the 48-hr forecast when G2S data are used. On the other hand, when the model is initialized using balanced flow, the zonal wind is horizontally smooth in the 1-hr forecast, and no small-scale noises seem to grow with time. Consequently, it is confirmed that the iterative dynamic initialization allows for dynamical balance among the model's prognostic variables and reduces excitation of spurious GWs and noises at initial time.

4.5. Examination of the Degree of Theoretical Balance

In this subsection, we examine how much the flow balanced with respect to the primitive equation model satisfies a theoretical balance equation that is a diagnostic relation between the velocity and mass fields for the large-scale motions (Houghton, 1968; Kasahara, 1982). Among various balance equations, the classical nonlinear balance equation in the spherical coordinate (Houghton, 1968) is written as

$$\nabla^2\Phi - f\nabla^2\psi = 2J(\tilde{u},\tilde{v}) - \beta\tilde{u} - \frac{1}{a\cos\phi}\frac{\partial}{\partial\phi}\left(\frac{\tilde{u}^2+\tilde{v}^2}{a}\sin\phi\right), \tag{12}$$

where $\tilde{u}$ and $\tilde{v}$ are the nondivergent zonal and meridional wind components computed from the stream function (ψ) and given by $-(1/a)\partial\psi/\partial\phi$ and $1/(a\cos\phi)\partial\psi/\partial\lambda$, respectively; λ is the longitude; β is the meridional gradient of the Coriolis parameter and given by $2\Omega\cos\phi/a$; and $J(\tilde{u},\tilde{v})$ is the Jacobian expressed as $1/(a^2\cos\phi)(\partial\tilde{u}/\partial\lambda\partial\tilde{v}/\partial\phi - \partial\tilde{u}/\partial\phi\partial\tilde{v}/\partial\lambda)$.

The classical balance equation is reduced to the well-known Monge-Ampère type nonlinear partial differential equation in ψ for a given Φ. For existence of its solution, the following ellipticity condition (Houghton, 1968; Kasahara, 1982) should be satisfied:

$$f^2 + 2\nabla^2\Phi + 2\beta\tilde{u} + 2\frac{\tilde{u}^2+\tilde{v}^2}{a} > 0. \tag{13}$$

In (12), nondivergent horizontal winds are only involved, but in more generalized balance equations, effects of horizontally divergent winds can be considered. Bourchtein and Bourchtein (2010) proposed a type of the generalized nonlinear balance equation where all the terms in the horizontal divergence equation except for the total time derivative of the divergence are retained (see their equation (9)). In this generalized form, the ellipticity condition is computed using the full (rotational and divergent) zonal and meridional wind components and written as

$$\begin{aligned} E = \left(\frac{f}{\cos\phi} - \frac{2}{a\cos\phi}\frac{\partial u}{\partial\phi}\right)\left(f\cos\phi + \frac{2}{a}\frac{\partial u}{\partial\lambda} + \frac{2u\sin\phi}{a}\right) - \\ \left(\frac{1}{a\cos\phi}\frac{\partial u}{\partial\lambda} - \frac{1}{a}\frac{\partial v}{\partial\phi} - \frac{v\tan\phi}{a}\right)^2 > 0. \end{aligned} \tag{14}$$

Here note that u and v are used instead of $\tilde{u}$ and $\tilde{v}$, respectively.

Figure 12 demonstrates the ellipticity (E) of the generalized nonlinear balance equation at $z = 10$, 54.6, and 80 km in G2S and balanced flow generated using $\tau = 24$ hr for 0000 UT on 1 December 2014. Nonelliptic regions ($E < 0$) are mostly found in the tropics and subtropics where the linear balance (geostrophic balance), a reasonable low-order approximation of the nonlinear balance, is not expected to hold due to small magnitude of f. In the midlatitude upper troposphere ($z = 10$ km), the ellipticity condition is satisfied in most regions except for some areas associated with the sharp horizontal gradients of the strong eastward jets (see Figure 9). These upper-tropospheric nonelliptic areas are found in both G2S and balanced flow. Near the stratopause ($z = 54.6$ km), areas of nonelliptic areas are quite reduced compared with the troposphere but still found along narrow and elongated regions around 40–50°N related to the large horizontal gradients of the planetary-scale eastward jets (see Figure 9). As in the troposphere, these nonelliptic regions are found in both G2S and balanced flow near the stratopause. In the upper mesosphere ($z = 80$ km), however, there are significant differences between G2S and balanced flow. Nonelliptic areas are confined in the tropics for G2S, whereas they are widespread in the subtropics and midlatitudes around the westward jets as well as the eastward jets in balanced flow. This complicated ellipticity structure in balanced flow may be related to the

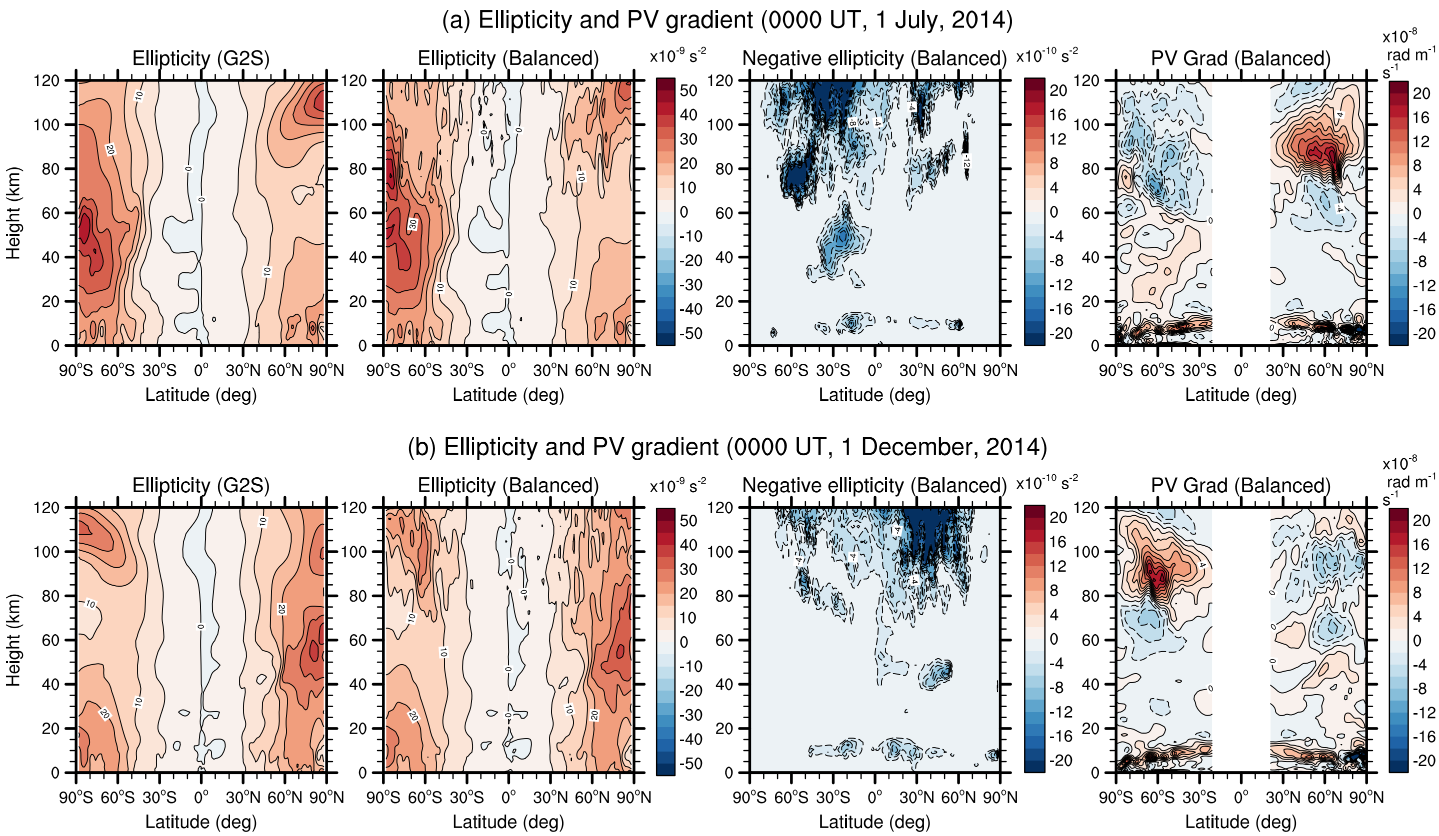

Figure 13. Latitude-height cross sections of the zonal-mean ellipticity (E) of the nonlinear balance equation in the G2S data and the zonal-mean ellipticity, zonally averaged negative ellipticity, and meridional gradient of the mean-flow quasi-geostrophic PV in the balanced flow generated using τ = 24 hr for (a) 0000 UT on 1 July 2014 and for (b) 0000 UT on 1 December 2014. The zonal-mean negative ellipticity is obtained by averaging the negative values of E in the zonal direction. Contour intervals for the ellipticity, negative ellipticity, and PV are 5×10^{-9} s^{-2}, 2×10^{-10} s^{-2}, and 2×10^{-8} rad·s^{-1}·m^{-1}, respectively. Contour lines for negative values are plotted in dashed lines. G2S = ground-to-space; PV = potential vorticity.

large-scale instabilities in that this structure correlates well with nearby negative meridional gradients of the mean PV. Details will be presented in the next section.

Balanced flow shown in Figure 12 is generated considering the local time changes of G2S wind and temperature. Without the local time changes, the tropospheric nonelliptic areas are significantly smoothed out compared with G2S (see Figure S10). This result indicates that considering the local time changes of the analysis data improves realism of balanced flow generated in this study. The upper-tropospheric nonelliptic areas may be related to the spontaneous generation of GWs from the jet flow (e.g., Plougonven & Zhang, 2014; Vanneste, 2013). In a viewpoint of NWP where the prediction of slowly varying flows is of major concern, the balanced flow, defined based on the PV field (McIntyre, 2015a), might be expected to keep slowly varying and uncontaminated by fast GW oscillations, staying in a phase space called the invariant slow manifold (Leith, 1980; Lorenz, 1980, 1986). Existence of the invariant slow manifold, however, has long been argued. Relevant studies have shown that it may be unavoidable for the slowly varying balanced flow to spontaneously excite GWs (see Vanneste, 2013, and references therein). That is, balanced flow in this study is obtained as if it is slowly varying and free from spurious GWs as seen in Figure 10, but as the model proceeds in time from balanced flow, flows may indispensably accompany GWs that are spontaneously generated from balanced flow.

5. Discussion

There have been studies on the large-scale instability in the summer mesosphere and the winter stratopause (e.g., Simmons, 1974; 1977). It is known that the large-scale instability can induce traveling planetary waves such as the quasi 2-day and 4-day waves that can have substantial impacts in the MLT dynamics (e.g., Manney & Randel, 1993; Plumb, 1983; Randel & Lait, 1991). In terms of the stability analysis, the large-scale instability is often examined using its necessary condition (Andrews et al., 1987) that the meridional gradient of the zonal-mean quasi-geostrophic (QG) PV becomes negative somewhere in a region where the instability occurs:

$$\frac{\partial \bar{q}}{\partial y} = \beta - \frac{\partial^2 \bar{u}}{\partial y^2} - \frac{1}{\rho_0}\frac{\partial}{\partial z}\left(\rho_0 \frac{f^2}{N^2}\frac{\partial \bar{u}}{\partial z}\right) < 0 \text{ somewhere in a region of interest,} \tag{15}$$

where $\bar{q}$ is the zonal-mean QG PV; N is the log-pressure stability given by $RH^{-1}\partial\bar{\theta}/\partial z e^{-\kappa z/H}$; and $\kappa = R/c_p$.

Figure 13 shows latitude-height cross sections of the zonal-mean ellipticity (E) of the nonlinear balance equation in G2S data and the zonal-mean E, zonally averaged negative E, and $\partial\bar{q}/\partial y$ in balanced flow generated using $\tau = 24$ hr for 0000 UT on 1 July 2014 and 1 December 2014. The zonal-mean E is generally positive in the midlatitude regions in both G2S and balanced flow, but it is substantially reduced in the midlatitude MLT region in case of balanced flow. Small E in balanced flow in the MLT region indicates large values of negative E over wide areas. Near the stratopause, small negative Es are found in winter (20–40°S in July, and 40–50°N in December), although their correlation with nearby negative $\partial\bar{q}/\partial y$s is not clear in July. On the other hand, in the mesosphere, correlation between negative E and neighboring negative $\partial\bar{q}/\partial y$ seems clear regardless of seasons. In the winter mesosphere, the correlation is large in the regions of the large negative $\partial\bar{q}/\partial y$ around 40–70°S at $z = 65$–80 km in July, and weak correlation is found along regions of the small negative $\partial\bar{q}/\partial y$s around 30–70°N at $z = 70$–80 km in December. In the summer mesosphere, large positive $\partial\bar{q}/\partial y$s are found in the upper mesosphere, and it is surrounded by negative $\partial\bar{q}/\partial y$s in the lower mesosphere and lower thermosphere. Correlation between negative E and neighboring negative $\partial\bar{q}/\partial y$s is clear along the lower and upper boundaries of the positive $\partial\bar{q}/\partial y$ region. In the lower thermosphere, negative E is large, which may be related to the violation of the QG balance due to tidal motions nudged through G2S data (Fuller-Rowell, 1995).

The negative Es near the winter stratopause in July do not seem clearly related to the large-scale instability, but it may be related to the spontaneous generation of GWs in the region of the strong polar night jets, similar to the tropospheric case shown in Figure 12. Note that E is mostly positive in the midlatitude troposphere. Spontaneous GW generation near the winter stratopause can be a potentially important source mechanism for GWs that can affect the large-scale flow in the MLT region. In the mesosphere, correlations between the negative E and nearby negative $\partial\bar{q}/\partial y$ are clear, which indicates that GWs can possibly be generated by the unbalanced large-scale instabilities in the mesosphere (see Plougonven & Zhang, 2014; Vanneste, 2013). The unbalanced instability is in contrast to the balanced instability. The former can be examined using the full primitive equation set as in this study, but the latter has been investigated using the balanced QG equation set. As mentioned above, traveling planetary-scale waves such as the quasi-two-day and 4-day waves have been attributed to the balanced large-scale instability in the summer mesosphere or in the winter stratopause. In addition to the traveling planetary waves due to the balanced instability, as Figure 13 indicates, GWs due to the unbalanced instability in the mesosphere may also be important dynamical phenomena that can affect the large-scale flow in the MLT region.

6. Summary and Conclusion

This study presents a method of initializing a whole atmospheric global model by iteratively nudging the global model toward atmospheric data at specific date and time. For whole-atmosphere modeling, atmospheric analysis data to be used for initialization are usually expected to cover the entire model atmosphere. However, the spatiotemporal coverage and resolution of such data above the lower mesosphere are still substantially limited. To overcome this issue, we construct the G2S wind and temperature data based on the data fusion method. G2S data are used for the initialization of the whole-atmosphere model and obtained by combining the meteorological analysis data such as the ERA-Interim and MERRA data below the lower mesosphere and results of empirical models such as HWM14, DWM07, and NRLMSISE-00 above the stratopause.

In conventional dynamic initialization, nudging time scale has often been empirically chosen. In this study, nudging time scale is determined in a physically based way by examining if reasonable structure of mesospheric GW momentum forcing and residual mean meridional circulations can be obtained from balanced initial conditions. GW momentum forcing in the mesosphere is estimated based on modeling experiences that the atmospheric flow in the MLT region is largely in a state where GW momentum forcing is balanced by the Coriolis force, curvature term, and meridional advection and eddy transport term. For the nudging time scale of about 24 hr, estimated mesospheric GW momentum forcing is found to exhibit a distinctive and reasonable structure with larger (smaller) values in the lower and upper mesosphere (in the midmesosphere), compared with parameterized climatological forcing. For the same nudging time scale, the summer-to-winter residual mean meridional flow is found to exist in a deep layer throughout the middle to upper mesosphere.

The iterative dynamic initialization presented in this study allows for dynamical balance among the model's prognostic variables and reduces excitation of spurious GWs at initial time. For realistic and long-term simulations of the whole atmosphere and for comparison with observations, modeling studies have often employed a so-called specified dynamics (SD) approach (e.g., Marsh, 2011) that nudges models in time toward sequence of atmospheric analysis data below the lower mesosphere. If we are only interested in slowly varying upper-atmospheric large-scale flows, which can be obtained using the SD approach, generation of the balanced flow as in the present study might be unnecessary. Yet the SD approach is not appropriate in case that explicit simulations for mesoscale GWs excited from the lower atmosphere are required, since model-resolved GWs may be modulated or eliminated from the lower atmosphere in the coarse of time integration by nudging terms used in the SD approach. The dynamical balance in this study is related to determining the model's initial conditions and to deterministic model runs from balanced initial conditions, as shown in Figure 11. Deterministic high-resolution model runs from balanced initial conditions generated in this study may allow for explicit simulations of mesoscale GWs propagating from the troposphere to the upper atmosphere.

In this study, we generate the flow balanced with respect to a model using the iterative dynamic initialization method rather than the balanced flow theoretically defined based on the PV concept. Although the generated balanced flow initially seems slowly varying and free of spurious GW oscillations, theoretical imbalances, measured by the ellipticity of the nonlinear balance equation, are not completely eliminated. Those imbalances are found in the tropospheric jet regions, in the winter stratopause regions, and in local areas associated with the large-scale instability spread throughout the midlatitude MLT region. In the troposphere and near the stratopause, these imbalances seem irrelevant to the large-scale instability, and they may be related to the spontaneous generation of GWs from balanced flow. In the mesosphere, the imbalances correlate well with the nearby large-scale instability, and they may be potentially related to generation of mesospheric GWs due to unbalanced large-scale instability.

Appendix A : Construction of G2S Atmospheric Profiles

Vertically continuous G2S atmospheric profiles at specific date and time are made through the following procedures: (i) The variables (u, v, T, and qs) are assumed to be horizontally gridded as in the ERA-Interim (0.75° latitude $\times$ 0.75° longitude). Therefore, for the MERRA data, the variables are linearly interpolated in the default ERA-Interim horizontal grid. (ii) For u, v, and T above 1 hPa, the NRLMSISE-00 model (subroutine GHP7) is first computed to obtain the temperature (T) and geopotential heights at the ERA-Interim horizontal grid and 46 predefined pressure levels (five levels per decade change in pressure) from 1 hPa to 10^{-9} hPa ($\approx$ 500 km). Then, the HWM14 (and DWM07) is computed as a function of the geopotential heights (the output of the GHP7) obtained at the same predefined pressure levels to obtain the horizontal wind components (u and v). (iii) Smooth curves represented by a linear combination of the third-order B-spline functions (see Chap. 9.4.1 in Piegl & Tiller, 1997) are, in a least squares sense, fit in the vertical direction to the reanalysis data and empirical model results at the ERA-Interim horizontal grid points. In the layer of 400–1 hPa (1–0.1 hPa), both the ERA-Interim and MERRA data (both the MERRA and empirical model results) are available and used together in the spline fit. The smooth curves are defined at 100 final pressure levels from 10^3 to 10^{-9} hPa. The final pressure levels are gradually stretched with height. There are 35, 54, and 100 levels below 10^2, 1, and 10^{-9} hPa, respectively. Between 1 and 10^{-9} hPa, the final pressure levels are identical to the levels used for the empirical models. The number and positions of the basis spline functions are adaptively determined based on maximum and root-mean-square tolerances following algorithms by Dill (2004). In the original G2S specification (Drob et al., 2003), the B-spline fit is carried out for spherical harmonic coefficients, whereas in this study, the fit is simply achieved using values in the physical domain. Using spectral coefficients may allow for the more precise fit, but using values in the physical domain also appears to yield reasonable results (see Figures 1 and 2).

Appendix B : Time Integration of Dynamical Model

Time integration of the SE core is carried out in multiple stages called subcycles for a given physics time step (Δt) at which the physics forcing ($\boldsymbol{P_u}$ and P_T) is applied. The subcycle procedure is summarized as follows: (i) The dynamical equations (1)–(3) for $\boldsymbol{u}$, T, and δp (the pressure depth between two adjacent η levels) are N_q times integrated using a dynamic time step δt ($< \Delta t$) based on the vertically Lagrangian approach (Lin, 2004), ignoring the vertical advection terms that include $\dot{\eta}$. First integration for δt is achieved using a second-order Runge-Kutta (RK2) method, and the later $N_q - 1$ integrations are computed using the leapfrog method. The terms Φ and ω in (1) and (2) are diagnostically obtained (see Dennis et al., 2012, for details). After every integration for δt, horizontal diffusion for the dynamic variable ξ ($\boldsymbol{u}$, T, and δp) is computed using the hyperviscosity term given by $\nu \nabla^4 \xi$, where ν is the viscosity coefficient. Horizontal momentum diffusion is enhanced when the divergence is strong. Given that the Laplacian (∇^2) of the horizontal wind vector can be represented as a linear combination of the divergence and vorticity terms, enhancement of the diffusion for the divergent flow is implemented in a way of increasing the contribution of the divergence in the Laplacian by a given factor of $\nu_{\rm div}/\nu$ (> 1) (i.e., $\nabla^2 \boldsymbol{u} \approx -\left[\boldsymbol{\nabla} \times (\zeta \boldsymbol{k}) - \nu_{\rm div}/\nu\, \boldsymbol{\nabla}(\boldsymbol{\nabla} \cdot \boldsymbol{u})\right]$). (ii) Equations for tracers (4) are integrated for the time period of $N_q \delta t$ using a three-stage second-order accurate RK Strong-Stability-Preserving method (Spiteri & Ruuth, 2002), neglecting the vertical advection terms as well. A limiter is applied in the tracer equations to preserve the monotonicity (Taylor et al., 2009). (iii) The steps of (i) and (ii) are repeated N_r times. (iv) Effects of the vertical advection in (1)–(4) are computed through vertical remapping. The remap of dynamical variables ($\boldsymbol{u}$, T, and δp) and tracers ($q\delta p$) is achieved as suggested in Lin (2004) using the algorithm by Zerroukat et al. (2005). Finally, (v) the steps of (i)–(iv) are repeated N_n times. As a result of this subcycling, the dynamical time step (δt) is determined as $\Delta t/(N_q N_r N_n)$.

In this study, the horizontal resolution of the CS grid is chosen so that it can divide each face of the cube into 30×30 elements (i.e., 30×30 small rectangular areas) of which each contains 4×4 Gauss-Lobatto-Legendre quadrature points. This grid approximately corresponds to the $1° \times 1°$ lat-long grid. For this resolution, we use Δt of 15 min, (N_q, N_r, N_n) of (4, 2, 5), and thus δt becomes 22.5 s. For the N_q time integrations of (1)–(3), the Courant-Friedrichs-Lewy condition is close to $N_q - 1$, and the value of 4 or 5 is typically chosen for N_q (Dennis et al., 2012). The vertical remap is computed every $N_r N_q \delta t$ s. Frequent remap can be helpful in model stability. Therefore, for a given N_q, the use of a small value of N_r can give better stability. The values of N_r and N_n (2 and 5) are appropriately chosen considering model stability for a relatively large dynamic time step ($\delta t = 22.5$ s). For the horizontal diffusion, ν and $\nu_{\rm div}$ are set equal to 10^{15} and 2.5×10^{15} m^4/s, respectively. We use the 66 vertical layers for simulations from the ground to the lower thermosphere as in WACCM.

Acknowledgments
The authors would like to express appreciation for valuable comments from three anonymous reviewers. Reviewer comments substantially helped improve the original manuscript. This study was supported by research fund PE18020 from Korea Polar Research Institute and funded by the KMA/NMSC's (Korea Meteorological Administration/National Meteorological Satellite Center) project (NMSC-2016-3137). Also, this work was supported by the National Institute of Supercomputing and Network/Korea Institute of Science and Technology Information with supercomputing resources including technical support (KSC-2015-C3-025). ERA-Interim data are available through http://apps.ecmwf.int. MERRA products are available through http://disc.sci.gsfc.nasa.gov/daac-bin/DataHolings.pl. HWM14 model is available as a part of the supporting information of Drob et al. (2015) at http://onlinelibrary.wiley.com/doi/10.1002/2014EA0000089. DWM07 and NRLMSISE-00 models are available through http://ccmc.gsfc.nasa.gov/modelweb. The $F_{10.7}$ and Ap indices (measures for solar and geomagnetic activities) used as input parameters to the HWM14, DWM07, and NRLMSISE-00 models can be obtained from the National Centers for Environmental Information (NCEI) at ftp://ftp.ngdc.noaa.gov/STP/GEOMAGNETIC_DATA/INDICES/KP_AP. NOAA Optimum Interpolation (OI) SST version 2 data provided by Physical Sciences Division (PSD) at NOAA Earth System Research Laboratory (ESRL) are available at https://www.esrl.noaa.gov/psd.

References

Akmaev, R. A. (2011). Whole atmosphere modeling: Connecting terrestrial and space weather. *Reviews of Geophysics*, *49*, RG4004. https://doi.org10.1029/2011RG000364

Anderson, C., Davies, T., Conde, M., Dyson, P., & Kosch, M. J. (2011). Spatial sampling of the thermospheric vertical wind field at auroral latitudes. *Journal of Geophysical Research*, *116*, A06320. https://doi.org10.1029/2011JA016485

Andrews, D. G., Holton, J. R., & Leovy, C. B. (1987). *Middle Atmosphere Dynamics*. San Diego, CA: Academic Press.

Auroux, D., & Blum, J. (2008). A nudging-based data assimilation method: The Back and Forth Nudging (BFN) algorithm. *Nonlinear Processes in Geophysics*, *15*, 305–319. https://doi.org10.5194/npg-15-305-2008

Baer, F., & Tribbia, J. J. (1977). On complete filtering of gravity modes through nonlinear initialization. *Monthly Weather Review*, *105*, 1536–1539. https://doi.org10.1175/1520-0493(1977)105<1536:OCFOGM>2.0.CO;2

Bao, J. W., & Errico, R. M. (1997). An adjoint examination of a nudging method for data assimilation. *Monthly Weather Review*, *125*, 1355–1373. https://doi.org10.1175/1520-0493(1997)125<1355:AAEOAN>2.0.CO;2

Bloom, S. C., Takacs, L. L., da Silva, A. M., & Ledvina, D. (1996). Data assimilation using incremental analysis updates. *Monthly Weather Review*, *124*, 1256–1271. https://doi.org10.1175/1520-0493(1996)124<1256:DAUIAU>2.0.CO;2

Bosilovich, M., Akella, S., Coy, L., Cullather, R., Draper, C., Gelaro, R., et al. (2015). MERRA-2: Initial evaluation of the climate (NASA Tech. Rep.), Series on global modeling and data sssimilation, NASA/TM-2015-104606 (Vol. *43*). Greenbelt, Maryland: NASA Goddard Space Flight Center.

Bourchtein, A., & Bourchtein, L. (2010). On ellipticity of balance equations for atmospheric dynamics. *Journal of Computational and Applied Mathematics*, *234*, 1017–1026. https://doi.org10.1016/j.cam.2009.03.011

Brakebusch, M., Randall, C. E., Kinnison, D. E., Tilmes, S., Santee, M. L., & Manney, G. L. (2013). Evaluation of Whole Atmosphere Community Climate Model simulations of ozone during Arctic winter 2004–2005. *Journal of Geophysical Research: Atmospheres*, *118*, 2673–2688. https://doi.org10.1002/jgrd.50226

Burns, A. G., Wang, W., Solomon, S. C., & Qian, L. (2014). Energetics and composition in the thermosphere. In J. Huba, et al. (Eds.), *Modeling the Ionosphere-Thermosphere System* (pp. 39–48). Chichester, UK: John Wiley & Sons, Ltd. https://doi.org10.1002/9781118704417.ch4

Cacuci, D. G., Navon, I. M., & Ionescu-Bujor, M. (2014). Basic principles of 4-D VAR. In *Computational Methods for Data Evaluation and Assimilation* (pp. 183–225). Florida: CRC Press.

Charney, J. G., & Drazin, P. G. (1961). Propagation of planetary-scale disturbances from the lower into the upper atmosphere. *Journal of Geophysical Research*, *66*, 83–109. https://doi.org10.1029/JZ066i001p00083

Daley, R. (1991). *Atmospheric Data Analysis*. New York: Cambridge University Press.

Davies, H. C., & Turner, R. E. (1977). Updating prediction models by dynamical relaxation: An examination of the technique. *Quarterly Journal of the Royal Meteorological Society*, *103*, 225–245. https://doi.org10.1002/qj.49710343602

Dee, D. P., Uppala, S. M., Simmons, A. J., Berrisford, P., Poli, P., Kobayashi, S., et al. (2011). The ERA-Interim reanalysis: Configuration and performance of the data assimilation system. *Quarterly Journal of the Royal Meteorological Society*, *137*, 553–597. https://doi.org10.1002/qj.828

Deng, Y., & Ridley, A. J. (2012). The global ionosphere-thermosphere model and the non-hydrostatic processes. In *Modeling the Ionosphere-Thermosphere System, Geophysical Monograph Series* (Vol. 201, pp. 85–100). Washington, DC: American Geophysical Union https://doi.org10.1029/2012GM001296

Dennis, J. M., Edwards, J., Evans, K. J., Guba, O., Lauritzen, P. H., Mirin, A. A., et al. (2012). CAM-SE: A scalable spectral element dynamical core for the Community Atmospheric Model. *International Journal of High Performance Computing Applications*, *26*, 74–89. https://doi.org10.1177/1094342011428142

Dill, L. H. (2004). Representation of ice geometry by parametric functions: Construction of approximating NURBS curves and quantification of ice roughness—Year 1: Approximating NURBS curves (Tech. Rep. NASA/CR-2004-213071). Ohio: NASA Glenn Research Center.

Dolinar, E. K., Dong, X., & Xi, B. (2016). Evaluation and intercomparison of clouds, precipitation, and radiation budgets in recent reanalyses using satellite-surface observations. *Climate Dynamics*, *46*, 2123–2144. https://doi.org10.1007/s00382-015-2693-z

Drob, D. P., Emmert, J. T., Crowley, G., Picone, J. M., Shepherd, G. G., Skinner, W., et al. (2008). An empirical model of the Earth's horizontal wind fields: HWM07. *Journal of Geophysical Research*, *113*, A12304. https://doi.org10.1029/2008JA013668

Drob, D. P., Emmert, J. T., Meriwether, J. W., Makela, J. J., Doornbos, E., Conde, M., et al. (2015). An update to the Horizontal Wind Model (HWM): The quiet time thermosphere. *Earth and Space Science*, *2*, 301–319. https://doi.org10.1002/2014EA000089

Drob, D. P., Picone, J. M., & Garcés, M. (2003). Global morphology of infrasound propagation. *Journal of Geophysical Research*, *108*(D21), 4680. https://doi.org10.1029/2002JD003307

Dunkerton, T. (1978). On the mean meridional mass motions of the stratosphere and mesosphere. *Journal of the Atmospheric Sciences*, *35*, 2325–2333. https://doi.org10.1175/1520-0469(1978)035<2325:OTMMMM>2.0.CO;2

Durran, D. R. (1989). Improving the anelastic approximation. *Journal of the Atmospheric Sciences*, *46*, 1453–1461. https://doi.org10.1175/1520-0469(1989)046<1453:ITAA>2.0.CO;2

Durran, D. (2008). A physically motivated approach for filtering acoustic waves from the equations governing compressible stratified flow. *Journal of Fluid Mechanics*, *601*, 365–379. https://doi.org10.1017/S0022112008000608

Eckemann, S. D., Hoppel, K. W., Coy, L., McCormack, J. P., Siskind, D. E., Nielsen, K., et al. (2009). High-altitude data assimilation system experiments for the northern summer mesosphere season of 2007. *Journal of Atmospheric and Solar-Terrestrial Physics*, *71*, 531–551. https://doi.org10.1016/j.jastp.2008.09.036

Emmert, J. T., Drob, D. P., Shepherd, G. G., Hernandez, G., Jarvis, M. J., Meriwether, J. W., et al. (2008). DWM07 global empirical model of upper thermospheric storm-induced disturbance winds. *Journal of Geophysical Research*, *113*, A11319. https://doi.org10.1029/2008JA013541

Errico, R. (1982). Normal mode initialization and the generation of gravity waves by quasi-geostrophic forcing. *Journal of the Atmospheric Sciences*, *39*, 573–586. https://doi.org10.1175/1520-0469(1982)039<0573:NMIATG>2.0.CO;2

Forbes, J. M. (2007). Dynamics of the thermosphere. *Journal of the Meteorological Society of Japan*, *85B*, 193–213. https://doi.org10.2151/jmsj.85B.193

Ford, R., McIntyre, M. E., & Norton, W. A. (2000). Balance and the slow quasimanifold: Some explicit results. *Journal of the Atmospheric Sciences*, *57*, 1236–1254. https://doi.org10.1175/1520-0469(2000)057<1236:BATSQS>2.0.CO;2

Fujiwara, M., Wright, J. S., Manney, G. L., Gray, L. J., Anstey, J., Birner, T., et al. (2017). Introduction to the SPARC Reanalysis Intercomparison Project (S-RIP) and overview of the reanalysis systems. *Atmospheric Chemistry and Physics*, *17*, 1417–1452. https://doi.org10.5194/acp-17-1417-2017

Fuller-Rowell, T. J. (1995). The dynamics of the lower thermosphere. In R. M. Johnson & T. L. Killeen (Eds.), *The Upper Mesosphere and Lower Thermosphere: A Review of Experiment and Theory* (pp. 23–36). Washington, DC: American Geophysical Union. https://doi.org10.1029/GM087p0023

Fuller-Rowell, T. (2013). Physical characteristics and modeling of Earth's thermosphere. In J. Huba, et al. (Eds.), *Modeling the Ionosphere-Thermosphere System* (pp. 13–27). Chichester, UK: John Wiley & Sons, Ltd. https://doi.org10.1002/9781118704417.ch2

Haseler, J., & Sakellarides, G. (1986). Description of the ECMWF model post processing system (Tech. Memo. 121). UK.

Hedin, A. E. (1991). Extension of the MSIS thermosphere model into the middle and lower atmosphere. *Journal of Geophysical Research*, *96*, 1159–1172. https://doi.org10.1029/90JA02125

Hedin, A. E., Fleming, E. L., Manson, A. H., Schmidlin, F. J., Avery, S. K., Clark, R. R., et al. (1996). Empirical wind model for the upper, middle and lower atmosphere. *Journal of Atmospheric and Solar-Terrestrial Physics*, *58*, 1421–1447. https://doi.org10.1016/0021-9169(95)00122-0

Hoke, J. E., & Anthes, R. A. (1976). The initialization of numerical models by a dynamic-initialization technique. *Monthly Weather Review*, *104*, 1551–1556. https://doi.org10.1175/1520-0493(1976)104<1551:TIONMB>2.0.CO;2

Hoke, J. E., & Anthes, R. A. (1977). Dynamic initialization of a three-dimensional primitive-equation model of Hurricane Alma of 1962. *Monthly Weather Review*, *105*, 1266–1280. https://doi.org10.1175/1520-0493(1977)105<1266:DIOATD>2.0.CO;2

Hoskins, B. J., McIntyre, M. E., & Robertson, A. W. (1985). On the use and significance of isentropic potential vorticity maps. *Quarterly Journal of the Royal Meteorological Society*, *111*, 877–946. https://doi.org10.1002/qj.49711147002

Houghton, D. D. (1968). Derivation of the elliptic condition for the balance equation in spherical coordinates. *Journal of the Atmospheric Sciences*, *25*, 927–928. https://doi.org10.1175/1520-0469(1968)025<0927:DOTECF>2.0.CO;2

Kalnay, E. (2003). *Atmospheric Modeling, Data Assimilation, and Predictability*. New York: Cambridge University Press.

Kasahara, A. (1974). Various vertical coordinate systems used for numerical weather prediction. *Monthly Weather Review*, *102*, 509–522. https://doi.org10.1175/1520-0493(1974)102<0509:VVCSUF>2.0.CO;2

Kasahara, A. (1982). Significance of non-elliptic regions in balanced flows of the tropical atmosphere. *Monthly Weather Review*, *110*, 1956–1967. https://doi.org10.1175/1520-0493(1982)110<1956:SONERI>2.0.CO;2

Kawatani, Y., Hamilton, K., Miyazaki, K., Fujiwara, M., & Anstey, J. A. (2016). Representation of the tropical stratospheric zonal wind in global atmospheric reanalyses. *Atmospheric Chemistry and Physics*, *16*, 6681–6699. https://doi.org10.5194/acp-16-6681-2016

Krishnamurti, T. N., Xue, J., Bedi, H. S., Ingles, K., & Oosterhof, D. (1991). Physical initialization for numerical weather prediction over the tropics. *Tellus*, *43A*, 53–81. https://doi.org10.1034/j.1600-0870.1991.t01-3-00007.x

Lakshmivarahan, S., & Lewis, J. M. (2013). Nudging methods: A critical overview. In S. K. Park & L. Xu (Eds.), *Data assimilation for atmospheric, oceanic and hydrological applications* (Vol. II, pp. 27–57). Berlin, Germany: Springer-Verlag. https://doi.org10.1007/978-3-642-35088-7_2

Larsen, M. F., & Meriwether, J. W. (2012). Vertical winds in the thermosphere. *Journal of Geophysical Research*, *117*, A09319. https://doi.org10.1029/2012JA017843

Leith, C. E. (1980). Nonlinear normal mode initialization and quasi-geostrophic theory. *Journal of the Atmospheric Sciences*, *37*, 958–968. https://doi.org10.1175/1520-0469(1980)037<0958:NNMIAQ>2.0.CO;2

Lin, S.-J. (2004). A "vertically Lagrangian" finite-volume dynamical core for global models. *Monthly Weather Review*, *132*, 2293–2397. https://doi.org10.1175/1520-0493(2004)132<2293:AVLFDC>2.0.CO;2

Lipps, F. B., & Hemler, R. S. (1982). A scale analysis of deep moist convection and some related numerical calculations. *Journal of the Atmospheric Sciences*, *39*, 2192–2210. https://doi.org10.1175/1520-0469(1982)039<2192:ASAODM>2.0.CO;2

Liu, H.-L., Marsh, D. R., She, C.-Y., Wu, Q., & Xu, J. (2009). Momentum balance and gravity wave forcing in the mesosphere and lower thermosphere. *Geophysical Research Letters*, *36*, L07805. https://doi.org10.1029/2009GL037252

Long, D. L., Jackson, D. R., Thuburn, J., & Mathison, C. (2013). Validation of Met Office upper stratospheric and mesospheric analyses. *Quarterly Journal of the Royal Meteorological Society*, *139*, 1214–1228. https://doi.org10.1002/qj.2031

Lorenc, A. C. (1986). Analysis methods for numerical weather prediction. *Quarterly Journal of the Royal Meteorological Society*, *112*, 1177–1194. https://doi.org10.1002/qj.49711247414

Lorenc, A. C., Bell, R. S., & Macpherson, B. (1991). The Meteorological Office analysis correction data assimilation scheme. *Quarterly Journal of the Royal Meteorological Society*, *117*, 59–89. https://doi.org10.1002/qj.49711749704

Lorenz, E. N. (1980). Attractor sets and quasi-geostrophic equilibrium. *Journal of the Atmospheric Sciences*, *37*, 1685–1699. https://doi.org10.1175/1520-0469(1980)037<1685:ASAQGE>2.0.CO;2

Lorenz, E. N. (1986). On the existence of a slow manifold. *Journal of the Atmospheric Sciences*, *43*, 1547–1557. https://doi.org10.1175/1520-0469(1986)043<1547:OTEOAS>2.0.CO;2

Manney, G. L., & Randel, W. J. (1993). Instability at the winter stratopause: A mechanism for the 4-day wave. *Journal of the Atmospheric Sciences*, *50*, 3928–3938. https://doi.org10.1175/1520-0469(1993)050<3928:IATWSA>2.0.CO;2

Marsh, D. R. (2011). Chemical-dynamical coupling in the mesosphere and lower thermosphere (1st ed.). In M. A. Abdu, et al. (Eds.), *Aeronomy of the Earth's Atmosphere and Ionosphere, IAGA Special Sopron Book Ser* (Vol. 2, pp. 3–17). Dordrecht: Springer. https://doi.org10.1007/978-94-007-0326-1_1

McIntyre, M. E. (2015a). Balanced flow (2nd ed.). In G. R. North, et al. (Eds.), *Encyclopedia of Atmospheric Sciences* (pp. 298–303). London, UK: Academic Press. https://doi.org10.1016/B978-0-12-382225-3.00484-9

McIntyre, M. E. (2015b). Potential vorticity (2nd ed.). In G. R. North, et al. (Eds.), *Encyclopedia of Atmospheric Sciences* (pp. 375–383). London, UK: Academic Press. https://doi.org10.1016/B978-0-12-382225-3.00140-7

McLandress, C., Scinocca, J. F., Shepherd, T. G., Reader, M. C., & Manney, G. L. (2013). Dynamical control of the mesosphere by orographic and nonorographic gravity wave drag during the extended northern winters of 2006 and 2009. *Journal of the Atmospheric Sciences*, *70*, 2152–2169. https://doi.org10.1175/JAS-D-12-0297.1

Meraner, K., Schmidt, H., Manzini, E., Funke, B., & Gardini, A. (2016). Sensitivity of simulated mesospheric transport of nitrogen oxides to parameterized gravity waves. *Journal of Geophysical Research: Atmospheres*, *121*, 12,045–12,061. https://doi.org10.1002/2016JD025012

Nygård, T., Vihma, T., Birnbaum, G., Harmann, J., King, J., Lachlan-Cope, T., et al. (2016). Validation of eight atmospheric reanalyses in the Antarctic Peninsula region. *Quarterly Journal of the Royal Meteorological Society*, *142*, 684–692. https://doi.org10.1002/qj.2691

Pedatella, N. M., Raeder, K., Anderson, J. L., & Liu, H.-L. (2014). Ensemble data assimilation in the Whole Atmosphere Community Climate Model. *Journal of Geophysical Research: Atmospheres*, *119*, 9793–9809. https://doi.org10.1002/2014JD021776

Phillips, N. A. (1966). The equations of motion for a shallow rotating atmosphere and the "traditional approximation". *Journal of the Atmospheric Sciences*, *23*, 626–628. https://doi.org10.1175/1520-0469(1966)023<0626:TEOMFA>2.0.CO;2

Picone, J. M., Hedin, A. E., Drob, D. P., & Aikin, A. C. (2002). NRLMSISE-00 empirical model of the atmosphere: Statistical comparisons and scientific issues. *Journal of Geophysical Research*, *107*(A12), 1468. https://doi.org10.1029/2002JA009430

Piegl, L., & Tiller, W. (1997). *The NURBS Book*. Berlin, Germany: Springer-Verlag.

Plougonven, R., & Zhang, F. (2014). Internal gravity waves from atmospheric jets and fronts. *Reviews of Geophysics*, *52*, 33–76. https://doi.org10.1002/2012RG000419

Plumb, R. A. (1983). Baroclinic instability of the summer mesosphere: A mechanism for the quasi-two-day wave? *Journal of the Atmospheric Sciences*, *40*, 262–270. https://doi.org10.1175/1520-0469(1983)040<0262:BIOTSM>2.0.CO;2

Rančić, M., Purser, R. J., & Mesinger, F. (1996). A global shallow-water model using an expanded spherical cube: Gnomonic versus conformal coordinates. *Quarterly Journal of the Royal Meteorological Society*, *122*, 959–982. https://doi.org10.1002/qj.49712253209

Randall, C. E., Harvey, V. L., Holt, L. A., Marsh, D. R., Kinnison, D., Funke, B., & Bernath, P. F. (2015). Simulation of energetic particle precipitation effects during the 2003–2004 Arctic winter. *Journal of Geophysical Research: Space Physics*, *120*, 5035–5048. https://doi.org10.1002/2015JA021196

Randel, W. J., & Lait, L. R. (1991). Dynamics of the 4-day wave in the Southern Hemisphere polar stratosphere. *Journal of the Atmospheric Sciences*, *48*, 2496–2508. https://doi.org10.1175/1520-0469(1991)048<2496:DOTDWI>2.0.CO;2

Reynolds, R. W., Rayner, N. A., Smith, T. M., Stokes, D. C., & Wang, W. (2002). An improved in situ and satellite SST analysis for climate. *Journal of Climate*, *15*, 1609–1625. https://doi.org10.1175/1520-0442(2002)015<1609:AIISAS>2.0.CO;2

Rienecker, M. M., Suarez, M. J., Gelaro, R., Todling, R., Bacmeister, J., Liu, E., et al. (2011). MERRA: NASA's Modern-Era Retrospective Analysis for Research and Applications. *Journal of Climate*, *24*, 3624–3648. https://doi.org10.1175/JCLI-D-11-00015.1

Schunk, R. W. (2012). Ionosphere-thermosphere physics: Current status and problems. In *Modeling the Ionosphere-Thermosphere System, Geophysical Monograph Series* (Vol. 201, pp. 3–12). https://doi.org10.1029/2012GM001351

Schunk, R., & Nagy, A. (2009). *Ionospheres: Physics, Plasma Physics, and Chemistry* (2nd ed.). New York: Cambridge University Press.

Simmons, A. J. (1974). Baroclinic instability at the winter stratopause. *Quarterly Journal of the Royal Meteorological Society*, *100*, 531–540. https://doi.org10.1002/qj.49710042603

Simmons, A. J. (1977). Baroclinic instability in the summer mesosphere. *Quarterly Journal of the Royal Meteorological Society*, *103*, 211–215. https://doi.org10.1002/qj.49710343515

Simmons, A. J., & Burridge, D. M. (1981). An energy and angular-momentum conserving vertical finite-difference scheme and hybrid vertical coordinates. *Monthly Weather Review*, *109*, 758–766. https://doi.org10.1175/1520-0493(1981)109<0758:AEAAMC>2.0.CO;2

Siskind, D. E., Sassi, F., Randall, C. E., Harvey, V. L., Hervig, M. E., & Bailey, S. M. (2015). Is a high-altitude meteorological analysis necessary to simulate thermosphere-stratosphere coupling? *Geophysical Research Letters*, *42*, 8225–8230. https://doi.org10.1002/2015GL065838

Smith, A. K. (2003). The origin of stationary planetary waves in the upper mesosphere. *Journal of the Atmospheric Sciences*, *60*, 3033–3041. https://doi.org10.1175/1520-0469(2003)060<3033:TOOSPW>2.0.CO;2

Smith, A. K. (2012). Global dynamics of the MLT. *Surveys in Geophysics*, *33*, 1177–1230. https://doi.org10.1007/s10712-012-9196-9

Smith, R. W., & Hernandez, G. (1995). Vertical winds in the thermosphere within the polar cap. *Journal of Atmospheric and Solar-Terrestrial Physics*, *57*, 611–620. https://doi.org10.1016/0021-9169(94)00101-S

Smith, K. L., Neely, R. R., Marsh, D. R., & Polvani, L. M. (2014). The Specified Chemistry Whole Atmosphere Community Climate Model (SC-WACCM). *Journal of Advances in Modeling Earth Systems*, *6*, 883–901. https://doi.org10.1002/2014MS000346

Smolarkiewicz, P. K., Kühnlein, C., & Wedi, N. P. (2014). A consistent framework for discrete integrations of soundproof and compressible PDEs of atmospheric dynamics. *Journal of Computational Physics*, *263*, 185–205. https://doi.org10.1016/j.jcp.2014.01.031

Spiteri, R. J., & Ruuth, S. J. (2002). A new class of optimal high-order strong-stability-preserving time discretization methods. *SIAM Journal on Numerical Analysis*, *40*, 469–491. https://doi.org10.1137/S0036142901389025

Swinbank, R., & O'Neill, A. (1994). A stratosphere-troposphere data assimilation system. *Monthly Weather Review*, *122*, 686–702. https://doi.org10.1175/1520-0493(1994)122<0686:ASTDAS>2.0.CO;2

Tapping, K. E. (2013). The 10.7 cm solar radio flux ($F_{10.7}$). *Space Weather*, *11*, 394–406. https://doi.org10.1002/swe.20064

Taylor, M. (2011). Conservation of mass and energy for the moist atmospheric primitive equations on unstructured grids. In P. H. Lauritzen, et al. (Eds.), *Numerical Techniques for Global Atmospheric Models (Lecture Notes in Computational Science and Engineering* (Vol. 80, pp. 357–380). New York: Springer. https://doi.org10.1007/978-3-642-11640-7_12

Taylor, M. A., Edwards, J., & St.-Cyr, A. (2008). Petascale atmospheric models for the community climate system model: New developments and evaluation of scalable dynamical cores. *Journal of Physics: Conference Series*, *125*, 12023. https://doi.org10.1088/1742-6596/125/1/012023

Taylor, M., & Fournier, A. (2010). A compatible and conservative spectral element method on unstructured grids. *Journal of Computational Physics*, *229*, 5879–5895. https://doi.org10.1016/j.jcp.2010.04.008

Taylor, M. A., St.-Cyr, A., & Fournier, A. (2009). A non-oscillatory advection operator for the compatible spectral element method. In G. Allen, et al. (Eds.), *Computational Science ICCS 2009 Part II (Lecture Notes in Computer Science)* (Vol. 5545, pp. 273–282). Berlin: Springer. https://doi.org10.1007/978-3-642-11640-7_12

Taylor, M., Tribbia, J., & Iskandrani, M. (1997). The spectral element method for the shallow water equations on the sphere. *Journal of Computational Physics*, *130*, 92–108. https://doi.org10.1006/jcph.1996.5554

Telford, P., Braesicke, P., Morgenstern, O., & Pyle, J. A. (2008). Technical note: Description and assessment of a nudged version of the new dynamics Unified Model. *Atmospheric Chemistry and Physics*, *8*, 1701–1712. https://doi.org10.5194/acp-8-1701-2008

Vanneste, J. (2013). Balance and spontaneous wave generation in geophysical flows. *Annual Review of Fluid Mechanics*, *45*, 147–172. https://doi.org10.1146/annurev-fluid-011212-140730

Wang, H., Fuller-Rowell, T. J., Akmaev, R. A., Hu, M., Kleist, D. T., & Iredell, M. D. (2011). First simulations with a whole atmosphere data assimilation and forecast system: The January 2009 major sudden stratospheric warming. *Journal of Geophysical Research*, *116*, A12321. https://doi.org10.1029/2011JA017081

Warn, T., Bokhove, O., Shepherd, T. G., & Vallis, G. K. (1995). Rossby number expansions, slaving principles, and balance dynamics. *Quarterly Journal of the Royal Meteorological Society*, *121*, 723–739. https://doi.org10.1002/qj.49712152313

Warner, T. T. (2011). *Numerical Weather and Climate Prediction*. New York: Cambridge University Press.

White, A. A., Hoskins, B. J., Roulstone, I., & Staniforth, A. (2005). Consistent approximate models of the global atmosphere: Shallow, deep, hydrostatic, quasi-hydrostatic and non-hydrostatic. *Quarterly Journal of the Royal Meteorological Society*, *131*, 2081–2107. https://doi.org10.1256/qj.04.49

Zerroukat, M., Wood, N., & Staniforth, A. (2005). A monotonic and positive-definite filter for a semi-Lagrangian inherently conserving and efficient (SLICE) scheme. *Quarterly Journal of the Royal Meteorological Society*, *131*, 2923–2936. https://doi.org10.1256/qj.04.97

Zou, X., Navon, I. M., & Ledimet, F. X. (1992). An optimal nudging data assimilation scheme using parameter estimation. *Quarterly Journal of the Royal Meteorological Society*, *118*, 1163–1186. https://doi.org10.1002/qj.49711850808